

Homogenization estimates for fiber-reinforced elastomers with periodic microstructures

M. Brun^a, O. Lopez-Pamies^{a,b}, P. Ponte Castañeda^{a,b,*}

^a *LMS (CNRS UMR 7649), Département de Mécanique, École Polytechnique, 91128 Palaiseau, France*

^b *Department of Mechanical Engineering and Applied Mechanics, University of Pennsylvania, Philadelphia, PA 19104-6315, USA*

Received 5 December 2006; received in revised form 30 January 2007

Available online 8 February 2007

Abstract

This work presents a homogenization-based constitutive model for the mechanical behavior of elastomers reinforced with aligned cylindrical fibers subjected to finite deformations. The proposed model is derived by making use of the second-order homogenization method [Lopez-Pamies, O., Ponte Castañeda, P., 2006a. On the overall behavior, microstructure evolution, and macroscopic stability in reinforced rubbers at large deformations: I—theory. *J. Mech. Phys. Solids* 54, 807–830], which is based on suitably designed variational principles utilizing the idea of a “linear comparison composite.” Specific results are generated for the case when the matrix and fiber materials are characterized by generalized Neo-Hookean solids, and the distribution of fibers is *periodic*. In particular, model predictions are provided and analyzed for fiber-reinforced elastomers with Gent phases and square and hexagonal fiber distributions, subjected to a wide variety of three-dimensional loading conditions. It is found that for compressive loadings in the fiber direction, the derived constitutive model may lose strong ellipticity, indicating the possible development of macroscopic instabilities that may lead to kink band formation. The onset of shear band-type instabilities is also detected for certain in-plane modes of deformation. Furthermore, the subtle influence of the distribution, volume fraction, and stiffness of the fibers on the effective behavior and onset of macroscopic instabilities in these materials is investigated thoroughly.

© 2007 Elsevier Ltd. All rights reserved.

Keywords: Fiber-reinforced composite; Soft matter; Hyperelasticity; Stability; Microstructures; Homogenization

1. Introduction

The use of fiber-reinforced polymer matrix composites in engineering applications has steadily increased over the past several decades, primarily because of the high stiffness and strength-to-weight ratio, as well as the excellent fatigue and creep resistance over a broad range of temperatures, of these materials when compared to more conventional structural materials. In addition, fiber-reinforced-type morphologies appear

* Corresponding author. Address: Department of Mechanical Engineering and Applied Mechanics, University of Pennsylvania, Philadelphia, PA 19104-6315, USA. Tel.: +1 215 881 046; fax: +1 215 881 334.

E-mail addresses: brunmi@lms.polytechnique.fr (M. Brun), olp@seas.upenn.edu (O. Lopez-Pamies), ponte@seas.upenn.edu (P. Ponte Castañeda).

naturally in a number of other soft matter systems of increasing interest. An interesting example of such systems is that of thermoplastic elastomers in which the “hard” glassy phase self-assembles at a nanometer scale into aligned cylindrical fibers distributed *periodically*—in a hexagonal arrangement—in the “soft” rubbery phase (Honeker and Thomas, 1996; Honeker et al., 2000). Soft biological tissues such as arterial walls (Finlay et al., 1998), ligaments (Quapp and Weiss, 1998), and the annulus fibrosus of the human intervertebral disc (Skaggs et al., 1994), constitute additional examples of fiber-reinforced composites. Given that more often than not, fiber-reinforced “soft” materials—such as the ones mentioned above—are subjected to finite deformations, it is of practical interest to develop constitutive models for their mechanical behavior under such loading conditions. Beyond accounting for finite deformations, it is also desirable that these models incorporate full dependence on the constitutive behavior of the constituents (i.e., the matrix phase and the fibers), as well as on their spatial arrangement (i.e., the microstructure). In this work, we will focus on *hyperelastic* matrix and fiber phases. In addition, we will restrict attention to microgeometries with a single family of aligned fibers which are taken to be initially circular in cross section and *periodically* distributed in the undeformed configuration. The primary applications of models based on these (constitutive and geometric) hypotheses are the aforementioned class of thermoplastic elastomers, as well as tires.

There is a voluminous literature on *phenomenological* constitutive models for fibre-reinforced hyperelastic materials. In a pioneering contribution, Spencer (Spencer, 1972) idealized fibers as *inextensible* material line elements to develop a simple theory for *incompressible* fiber-reinforced materials that permitted the analytical treatment of numerous boundary value problems. Other (less idealized) phenomenological models are based on the idea of augmenting existing isotropic stored-energy functions with additional terms—which depend on the invariants associated with the fiber direction (Spencer, 1984)—that penalize deformation in a particular direction (see, e.g., Triantafyllidis and Abeyaratne, 1983; Qiu and Pence, 1997; Merodio and Ogden, 2005; Horgan and Saccomandi, 2005). The main appeal of these phenomenological models is that they are simple. In addition, they can be “calibrated” to become macroscopically unstable—via loss of strong ellipticity—for loading conditions where such instabilities are expected to occur from physical experience (see, e.g., Triantafyllidis and Abeyaratne, 1983; Merodio and Pence, 2001a,b; Merodio and Ogden, 2003). In spite of these desirable features, the predictive capabilities of phenomenological models for the general response of actual fiber-reinforced elastomers remain limited. Following a *micromechanics* approach, Guo et al. (2006) have recently proposed a hyperelastic model with incompressible Neo-Hookean matrix phases. In terms of *homogenization-based* methods, in addition to the microstructure-independent Voigt-type (Ogden, 1978) and Reuss-type (Ponte Castañeda, 1989) bounds, there are the estimates of Ponte Castañeda and Tiberio (2000) and Lahellec et al. (2004), which have the distinguishing feature of incorporating higher-order statistical information about the initial microstructure such as the fiber shape and distribution. More recently, deBotton et al. (2006) have derived an estimate for fiber-reinforced elastomers with incompressible Neo-Hookean phases and the special composite cylinder assemblage microstructure of Hashin (1962). One of the strengths of the model of deBotton et al. (2006) is that it is exact for axisymmetric and out-of-plane simple shear loading conditions. In passing, it should be mentioned that constitutive models for hyperelastic solids with orthotropic material symmetry have also been developed (Bischoff et al., 2002) from a *statistical mechanics* approach.

In this work, we will make use of the second-order homogenization theory—originally developed by Ponte Castañeda (2002) for viscoplastic materials, and extended recently for general hyperelastic composites by Lopez-Pamies and Ponte Castañeda (2006a)—to derive a constitutive model for the mechanical behavior of periodic fiber-reinforced elastomers. This technique has the capability to account for statistical information about the *initial* microstructure beyond the volume fraction, as well as for its *evolution*, which results from the finite changes in geometry that are induced by the applied finite deformations. This point is crucial as the evolution of the microstructure can have a significant *geometric* softening—or stiffening—effect on the overall response of the material, which, in turn, may lead to the possible development of macroscopic instabilities. The second-order homogenization theory has already been employed to generate constitutive models for *particle-reinforced* rubbers with random microstructures (Lopez-Pamies and Ponte Castañeda, 2006b), and for *porous* elastomers with random (Lopez-Pamies and Ponte Castañeda, 2004, in press-b) and periodic (Michel et al., in press) microstructures. These models have been shown to be in good agreement with corresponding exact and numerical results available from the literature for special loading conditions. More remarkably, they have been shown to predict the development of macroscopic instabilities for more general

conditions where such instabilities are expected to occur from physical experience, sometimes with great accuracy, as comparisons with F.E.M. solutions have demonstrated (Michel et al., in press). These encouraging results for such a variety of material systems strongly suggest that the second-order theory should also be able to deliver accurate estimates for the effective behavior, as well as for the onset of macroscopic instabilities, of the class of fiber-reinforced elastomers of interest in this work.

2. Preliminaries on periodic, fiber-reinforced, hyperelastic materials

Consider a material made up of aligned cylindrical fibers, which are distributed *periodically* in an elastic matrix phase. A specimen of this material is assumed to occupy a volume Ω_0 , with boundary $\partial\Omega_0$, in the undeformed configuration and to be such that the characteristic length-scale of the inhomogeneities (i.e., the average diameter of the fibers) is much smaller than the size of the specimen and the scale of variation of the applied loading.

Material points in the specimen are identified by their initial position vector \mathbf{X} in the reference configuration Ω_0 , while the current position of the same point is denoted by \mathbf{x} in the deformed configuration Ω . The deformation gradient tensor \mathbf{F} at \mathbf{X} , a quantity that measures the deformation in the neighborhood of \mathbf{X} , is defined as:

$$\mathbf{F} = \frac{\partial \mathbf{x}}{\partial \mathbf{X}}. \tag{1}$$

The constitutive behavior of the matrix and fibers is assumed to be purely elastic and characterized, respectively, by the stored-energy functions $W^{(1)}$ and $W^{(2)}$, which are taken to be *non-convex* functions of the deformation gradient tensor \mathbf{F} , so that the local energy function of the composite may be written as:

$$W(\mathbf{X}, \mathbf{F}) = \chi_0^{(1)}(\mathbf{X})W^{(1)}(\mathbf{F}) + \chi_0^{(2)}(\mathbf{X})W^{(2)}(\mathbf{F}). \tag{2}$$

Here, the characteristic functions $\chi_0^{(r)}$ ($r = 1, 2$), equal to 1 if the position vector \mathbf{X} is inside phase r (i.e., $\mathbf{X} \in \Omega_0^{(r)}$) and zero otherwise, describe the distribution of the phases (i.e., the microstructure) in the reference configuration. By exploiting the assumed periodicity of the microstructure, the fiber-reinforced elastomer can be thought of as the result of periodic repetition along each Cartesian coordinate direction \mathbf{e}_i ($i = 1, 2, 3$) of a fundamental building block D_0 —termed the *unit cell*. Taking D_0 to be a parallelepiped of dimension L_i along the direction \mathbf{e}_i , the initial distribution of the phases can thus be characterized (without loss of generality) by D_0 —periodic characteristic functions:

$$\chi_0^{(r)}(X_1, X_2, X_3) = \chi_0^{(r)}(X_1 + z_1L_1, X_2 + z_2L_2, X_3 + z_3L_3), \tag{3}$$

where z_1, z_2, z_3 are arbitrary integers. The usual (physically based) properties are assumed for the stored-energy functions of the phases. More specifically, the $W^{(r)}$ ($r = 1, 2$) are assumed to satisfy *material frame indifference*, namely, $W^{(r)}(\mathbf{Q}\mathbf{F}) = W^{(r)}(\mathbf{F})$ for all proper orthogonal tensors \mathbf{Q} and arbitrary deformation gradient \mathbf{F} , so that $W^{(r)}(\mathbf{F}) = W^{(r)}(\mathbf{U})$, where \mathbf{U} is the right stretch tensor in the polar decomposition $\mathbf{F} = \mathbf{R}\mathbf{U}$, and \mathbf{R} denotes the rotation tensor. Further, to try to ensure *material impenetrability*, it is assumed that $W^{(r)} \rightarrow \infty$ as $\det \mathbf{F} \rightarrow 0+$. In the Lagrangian description, the *local* or microscopic constitutive relation for the composite is then given by:

$$\mathbf{S} = \frac{\partial W}{\partial \mathbf{F}}(\mathbf{X}, \mathbf{F}), \tag{4}$$

where \mathbf{S} denotes the first Piola–Kirchhoff stress tensor, and sufficient smoothness has been assumed for W on \mathbf{F} .

Under the above-mentioned *separation of length-scales* hypothesis, the effective stored-energy function \tilde{W} of the fiber-reinforced elastomer is defined by (Hill, 1972):

$$\tilde{W}(\bar{\mathbf{F}}) = \min_{\mathbf{F} \in \mathcal{K}(\bar{\mathbf{F}})} \langle W(\mathbf{X}, \mathbf{F}) \rangle = \min_{\mathbf{F} \in \mathcal{K}(\bar{\mathbf{F}})} \sum_{r=1}^2 c_0^{(r)} \langle W^{(r)}(\mathbf{F}) \rangle^{(r)}, \tag{5}$$

where \mathcal{K} denotes the set of kinematically admissible deformation gradients:

$$\mathcal{K}(\bar{\mathbf{F}}) = \{ \mathbf{F} | \mathbf{x} = \boldsymbol{\chi}(\mathbf{X}) \quad \text{with } \mathbf{F} = \nabla \boldsymbol{\chi}, \det \mathbf{F} > 0 \text{ in } \Omega_0, \mathbf{x} = \bar{\mathbf{F}}\mathbf{X} \text{ on } \partial\Omega_0 \}. \tag{6}$$

In the above expressions, the triangular brackets $\langle \cdot \rangle$ and $\langle \cdot \rangle^{(r)}$ denote, respectively, volume averages—in the undeformed configuration—over the specimen (Ω_0) and over phase r ($\Omega_0^{(r)}$), so that the scalars $c_0^{(1)}$ and $c_0^{(2)}$ denote the initial volume fractions of the matrix and the fibers, respectively, in the undeformed configuration. Note also that \tilde{W} represents the average elastic energy stored in the fiber-reinforced elastomer when subjected to an affine displacement boundary condition that is consistent with $\langle \mathbf{F} \rangle = \bar{\mathbf{F}}$. Moreover, from the definition (5) and the objectivity of $W^{(1)}$ and $W^{(2)}$, it can be shown that \tilde{W} is objective, so that $\tilde{W}(\bar{\mathbf{F}}) = \tilde{W}(\bar{\mathbf{U}})$, where $\bar{\mathbf{U}}$ is the macroscopic right stretch tensor in the polar decomposition of the macroscopic deformation gradient $\bar{\mathbf{F}} = \bar{\mathbf{R}} \bar{\mathbf{U}}$, with $\bar{\mathbf{R}}$ denoting the macroscopic rotation tensor. (Note that $\bar{\mathbf{U}} \neq \langle \mathbf{U} \rangle$ and $\bar{\mathbf{R}} \neq \langle \mathbf{R} \rangle$.) It follows from the above formulation that the *global* or macroscopic constitutive relation for the composite is then given by:

$$\bar{\mathbf{S}} = \frac{\partial \tilde{W}}{\partial \bar{\mathbf{F}}}(\bar{\mathbf{F}}), \tag{7}$$

where $\bar{\mathbf{S}} = \langle \mathbf{S} \rangle$ is the *average stress* in the fiber-reinforced elastomer.

For hyperelastic composites with *periodic* microstructures, the variational problem (5) can be rewritten more explicitly (see Braides, 1985 and Müller, 1987) as follows:

$$\tilde{W}(\bar{\mathbf{F}}) = \inf_{\mathbf{k} \in \mathbb{Z}^3} \left\{ \min_{\mathbf{u}' \in \mathbf{k}D_{0\#}} \left\{ \frac{1}{|\mathbf{k}D_0|} \int_{\mathbf{k}D_0} W(\mathbf{X}, \bar{\mathbf{F}} + \nabla \mathbf{u}') d\mathbf{X} \right\} \right\}, \tag{8}$$

where \mathbb{Z}^3 denotes the set of all three-dimensional vectors $\mathbf{k} = (k_1, k_2, k_3)$ with integer components k_1, k_2, k_3 , and $\mathbf{k}D_{0\#}$ denotes the set of all $\mathbf{k}D_0$ —periodic fluctuation functions¹ \mathbf{u}' with $\int_{\mathbf{k}D_0} \nabla \mathbf{u}' d\mathbf{X} = \mathbf{0}$. (Note that in terms of the deformation field \mathbf{x} , the fluctuation field is given by $\mathbf{u}' = \mathbf{x} - \bar{\mathbf{F}}\mathbf{X}$, since $\langle \mathbf{F} \rangle = \bar{\mathbf{F}}$.) The infimum over all possible combinations of unit cells in (8) reveals explicitly the genuine character of *non-convex* local stored-energy functions W . Indeed, in this case, it is not sufficient to consider one-cell periodic solutions, as solutions involving interactions among several unit cells may lead to lower overall energies. Physically, this corresponds to accounting for the possible development of instabilities in the composite at sufficiently large deformations.

It is plain from (8) that the computation of \tilde{W} is a practically impossible task, in view of the infinity of the domain of definition (i.e., $\mathbf{k}D_0$ with $\mathbf{k} \in \mathbb{Z}^3$). For this reason, in this work, we adopt a more pragmatic approach. First, we note that by assuming—for consistency with the classical theory of linear elasticity—that $W^{(r)} = \frac{1}{2} \boldsymbol{\varepsilon} \cdot \mathbf{L}_{lin}^{(r)} \boldsymbol{\varepsilon} + o(\boldsymbol{\varepsilon}^3)$ ($r = 1, 2$) as $\mathbf{F} \rightarrow \mathbf{I}$, where $\boldsymbol{\varepsilon}$ denotes the infinitesimal strain tensor and $\mathbf{L}_{lin}^{(r)}$ ($r = 1, 2$) are positive-definite, constant, fourth-order tensors, it is expected (except for very special cases) that in the neighborhood of $\bar{\mathbf{F}} = \mathbf{I}$, the solution of the Euler–Lagrange equations associated with the variational problem (8) is unique, and gives the minimum energy. Furthermore, in the neighborhood of $\bar{\mathbf{F}} = \mathbf{I}$, the infimum in (8) is expected to be attained for $\mathbf{k} = (1, 1, 1)$, so that the one-cell minimization fluctuation field \mathbf{u}' is also the minimization fluctuation field for any super-cell $\mathbf{k}D_0$ (Müller, 1987). In short, for small enough deformations, $\tilde{W}(\bar{\mathbf{F}}) = \hat{W}(\bar{\mathbf{F}})$, where

$$\hat{W}(\bar{\mathbf{F}}) = \min_{\mathbf{u}' \in D_{0\#}} \left\{ \frac{1}{|D_0|} \int_{D_0} W(\mathbf{X}, \bar{\mathbf{F}} + \nabla \mathbf{u}') d\mathbf{X} \right\} \tag{9}$$

is the *one-cell effective stored-energy function* of the composite. In this last expression, $D_{0\#}$ denotes the set of all D_0 —periodic fluctuation functions \mathbf{u}' with $\int_{D_0} \nabla \mathbf{u}' d\mathbf{X} = \mathbf{0}$. By definition, it is clear that $\hat{W}(\bar{\mathbf{F}}) = \tilde{W}(\bar{\mathbf{F}})$ from $\bar{\mathbf{F}} = \mathbf{I}$ all the way up to the onset of the first instability, beyond which $\hat{W}(\bar{\mathbf{F}}) \geq \tilde{W}(\bar{\mathbf{F}})$. When this first instability happens to be of infinite long wavelength (i.e., *macroscopic*), Geymonat et al. (1993)—following the work of Triantafyllidis and Maker (1985)—have shown rigorously that the development of such an instability can be computed directly from the loss of strong ellipticity of \hat{W} . In this regard, it should also be mentioned that the loss of strong ellipticity of \hat{W} defines a “failure surface” that bounds all other types of instabilities in the solid (Triantafyllidis and Bardenhagen, 1996). Finally, and perhaps more importantly, it should be remarked that the computation of \hat{W} —as opposed to that of \tilde{W} —is tractable, as it amounts to solving a unit cell problem. Thus, in this work, we will not attempt to solve the variational problem (8), but instead, we will estimate the

¹ That is, functions satisfying $\mathbf{u}'(X_1, X_2, X_3) = \mathbf{u}'(X_1 + z_1 k_1 L_1, X_2 + z_2 k_2 L_2, X_3 + z_3 k_3 L_3)$ for all integers z_1, z_2, z_3 .

effective behavior—as well as the onset of macroscopic instabilities—of fiber-reinforced elastomers by means of the one-cell effective stored-energy function (9).

We conclude this section by spelling out the condition of strong ellipticity for the effective stored-energy function (9), which will be used in the sequel to detect the development of macroscopic instabilities in fiber-reinforced elastomers. Thus, the homogenized fiber-reinforced elastomer characterized by \hat{W} is said to be strongly elliptic if and only if²

$$\hat{B}(\bar{\mathbf{F}}) = \min_{\|\mathbf{m}\|=\|\mathbf{N}\|=1} \left\{ m_i N_j \hat{\mathcal{L}}_{ijkl}(\bar{\mathbf{F}}) m_k N_l \right\} > 0, \tag{10}$$

where $\hat{\mathcal{L}}(\bar{\mathbf{F}}) = \partial^2 \hat{W}(\bar{\mathbf{F}}) / \partial \bar{\mathbf{F}}^2$ is the effective incremental elastic modulus characterizing the overall incremental response of the fiber-reinforced elastomer. Note that loss of strong ellipticity, as detected from failure of condition (10), provides the critical deformation gradients, $\bar{\mathbf{F}}_{\text{crit}}$, at which the homogenized material becomes macroscopically unstable, as well as the pairs of unit vectors \mathbf{N} and \mathbf{m} for which these macroscopic instabilities occur. In particular, \mathbf{N} denotes the normal (in the undeformed configuration) to the surface of a weak or strong discontinuity of the deformation field, whereas \mathbf{m} characterizes the type of deformation associated with such a discontinuity (see, e.g., Knowles and Sternberg, 1975). For later use, it is also helpful to recall that the unit normal \mathbf{n} to the surface of discontinuity in the *deformed configuration* is given by $\mathbf{n} = \|\bar{\mathbf{F}}_{\text{crit}}^{-T} \mathbf{N}\|^{-1} \bar{\mathbf{F}}_{\text{crit}}^{-T} \mathbf{N}$ (see, e.g., Ogden, 1984).

3. Second-order estimates for periodic, fiber-reinforced, hyperelastic materials

Following the above framework, the main purpose of the present work is to generate an estimate for the effective stored-energy function (9) for fiber-reinforced elastomers consisting of a periodic distribution of monodisperse, initially circular, aligned cylindrical fibers in an isotropic, elastomeric matrix phase. A second objective is to provide estimates for the onset of macroscopic instabilities in these materials. This is accomplished here by means of the second-order homogenization method (Lopez-Pamies and Ponte Castañeda, 2006a). This method, which, as already stated, can be applied to large classes of hyperelastic composites, makes use of suitably designed variational principles utilizing the idea of a “linear comparison composite” (LCC) with the same microstructure as the original nonlinear composite (i.e., the same $\chi_0^{(1)}$ and $\chi_0^{(2)}$). For completeness, in this section, we recall briefly the essential components of the theory required to generate estimates for the type of materials of interest in this work.

Thus, making use of the general results of Lopez-Pamies and Ponte Castañeda (2006a) for two-phase composites, an estimate for the effective stored-energy function \hat{W} for the class of fiber-reinforced elastomers under investigation here, consisting of fibers with initial volume fraction $c_0^{(2)} = c_0$, characterized by the stored-energy function $W^{(2)}$, and distributed periodically in a compressible, isotropic matrix with stored-energy function $W^{(1)}$, may be generated in terms of a suitably designed fiber-reinforced LCC. Such LCC has matrix and fiber phases characterized, respectively, by:

$$W_T^{(1)}(\mathbf{F}) = W^{(1)}(\bar{\mathbf{F}}) + \mathcal{S}^{(1)}(\bar{\mathbf{F}}) \cdot (\mathbf{F} - \bar{\mathbf{F}}) + \frac{1}{2}(\mathbf{F} - \bar{\mathbf{F}}) \cdot \mathbf{L}^{(1)}(\mathbf{F} - \bar{\mathbf{F}}) \tag{11}$$

and

$$W_T^{(2)}(\mathbf{F}) = W^{(2)}(\bar{\mathbf{F}}^{(2)}) + \mathcal{S}^{(2)}(\bar{\mathbf{F}}^{(2)}) \cdot (\mathbf{F} - \bar{\mathbf{F}}^{(2)}) + \frac{1}{2}(\mathbf{F} - \bar{\mathbf{F}}^{(2)}) \cdot \mathbf{L}^{(2)}(\mathbf{F} - \bar{\mathbf{F}}^{(2)}), \tag{12}$$

and the same microstructure as the actual fiber-reinforced elastomer. In expression (11), $\mathcal{S}^{(1)}(\bar{\mathbf{F}}) = \partial W^{(1)}(\bar{\mathbf{F}}) / \partial \mathbf{F}$ and $\mathbf{L}^{(1)}$ is a constant, fourth-order tensor with major symmetry to be specified further below. On the other hand, in expression (12), $\mathcal{S}^{(2)}(\bar{\mathbf{F}}^{(2)}) = \partial W^{(2)}(\bar{\mathbf{F}}^{(2)}) / \partial \mathbf{F}$ and $\mathbf{L}^{(2)} = \partial^2 W^{(2)}(\bar{\mathbf{F}}^{(2)}) / \partial \mathbf{F}^2$, where $\bar{\mathbf{F}}^{(2)}$ is a second-order tensor that will also be specified subsequently. The corresponding effective stored-energy function for the just-defined LCC can be conveniently written (see, e.g., Lopez-Pamies and Ponte Castañeda, 2006a) as follows:

² Here and subsequently, unless otherwise indicated, lowercase Latin indices range from 1 to 3 and the usual summation convention is employed.

$$\hat{W}_T(\bar{\mathbf{F}}) = \tilde{f} + \tilde{\mathbf{T}} \cdot \bar{\mathbf{F}} + \frac{1}{2} \bar{\mathbf{F}} \cdot \tilde{\mathbf{L}} \bar{\mathbf{F}}, \quad (13)$$

where $\tilde{\mathbf{L}}$ is the effective modulus tensor of the linear comparison composite. In addition, in relation (13), $\tilde{f} = (1 - c_0)f^{(1)} + c_0f^{(2)} + \frac{1}{2}(\Delta\mathbf{L})^{-1}\Delta\mathbf{T} \cdot (\tilde{\mathbf{L}} - \bar{\mathbf{L}})(\Delta\mathbf{L})^{-1}\Delta\mathbf{T}$ and $\tilde{\mathbf{T}} = \bar{\mathbf{T}} + (\tilde{\mathbf{L}} - \bar{\mathbf{L}})(\Delta\mathbf{L})^{-1}\Delta\mathbf{T}$ with $f^{(1)} = \mathcal{W}^{(1)}(\bar{\mathbf{F}}) - \mathbf{T}^{(1)} \cdot \bar{\mathbf{F}} - \frac{1}{2}\bar{\mathbf{F}} \cdot \mathbf{L}^{(1)}\bar{\mathbf{F}}$, $f^{(2)} = \mathcal{W}^{(2)}(\bar{\mathbf{F}}^{(2)}) - \mathbf{T}^{(2)} \cdot \bar{\mathbf{F}}^{(2)} - \frac{1}{2}\bar{\mathbf{F}}^{(2)} \cdot \mathbf{L}^{(2)}\bar{\mathbf{F}}^{(2)}$, $\mathbf{T}^{(1)} = \mathcal{S}^{(1)}(\bar{\mathbf{F}}) - \mathbf{L}^{(1)}\bar{\mathbf{F}}$, and $\mathbf{T}^{(2)} = \mathcal{S}^{(2)}(\bar{\mathbf{F}}^{(2)}) - \mathbf{L}^{(2)}\bar{\mathbf{F}}^{(2)}$. Note that the notations $\Delta\mathbf{L} = \mathbf{L}^{(1)} - \mathbf{L}^{(2)}$ and $\bar{\mathbf{L}} = (1 - c_0)\mathbf{L}^{(1)} + c_0\mathbf{L}^{(2)}$ —and similarly for $\Delta\mathbf{T}$ and $\bar{\mathbf{T}}$ —have been introduced in the above expressions for convenience.

Having identified the local and effective behavior of the LCC, the second-order estimate for the effective stored-energy function \hat{W} may finally be written as:

$$\hat{W}(\bar{\mathbf{F}}) = (1 - c_0) \left[\mathcal{W}^{(1)}(\hat{\mathbf{F}}^{(1)}) - \mathcal{S}^{(1)}(\bar{\mathbf{F}}) \cdot (\hat{\mathbf{F}}^{(1)} - \bar{\mathbf{F}}^{(1)}) \right] + c_0 \mathcal{W}^{(2)}(\bar{\mathbf{F}}^{(2)}), \quad (14)$$

where the variables $\hat{\mathbf{F}}^{(1)}$, $\bar{\mathbf{F}}^{(1)}$, and $\bar{\mathbf{F}}^{(2)}$ are functions—of the applied loading $\bar{\mathbf{F}}$, the material properties of the matrix and fibers, and the initial microstructure—that must be determined from the above-defined LCC. More specifically, $\bar{\mathbf{F}}^{(1)}$ corresponds to the average deformation gradient in the matrix phase of the LCC, and can be conveniently expressed in terms of the average deformation gradient in the fibers of the LCC, $\bar{\mathbf{F}}^{(2)}$, from the global condition:

$$\bar{\mathbf{F}}^{(1)} = \frac{1}{1 - c_0} (\bar{\mathbf{F}} - c_0 \bar{\mathbf{F}}^{(2)}). \quad (15)$$

The average deformation gradient $\bar{\mathbf{F}}^{(2)}$ can be determined—in terms of the modulus tensor $\mathbf{L}^{(1)}$ —from the following *implicit* tensorial equation:

$$\bar{\mathbf{F}}^{(2)} = \bar{\mathbf{F}} - \frac{1}{c_0} (\Delta\mathbf{L})^{-1} (\tilde{\mathbf{L}} - \bar{\mathbf{L}}) (\Delta\mathbf{L})^{-1} [\Delta\mathcal{S} - \mathbf{L}^{(2)}(\bar{\mathbf{F}} - \bar{\mathbf{F}}^{(2)})], \quad (16)$$

where $\Delta\mathcal{S} = \mathcal{S}^{(1)}(\bar{\mathbf{F}}) - \mathcal{S}^{(2)}(\bar{\mathbf{F}}^{(2)})$. Finally, the variable $\hat{\mathbf{F}}^{(1)}$ is defined by the “generalized secant” condition:

$$\mathcal{S}^{(1)}(\hat{\mathbf{F}}^{(1)}) - \mathcal{S}^{(1)}(\bar{\mathbf{F}}) = \mathbf{L}^{(1)}(\hat{\mathbf{F}}^{(1)} - \bar{\mathbf{F}}). \quad (17)$$

Note that as it stands, the estimate (14) for \hat{W} is completely specified in terms of the modulus tensor $\mathbf{L}^{(1)}$ of the matrix phase of the LCC. From the general theory, this modulus tensor is obtained from a variational approximation for \hat{W} , where $\mathbf{L}^{(1)}$ plays the role of trial field. Optimizing such variational approximation with respect to $\mathbf{L}^{(1)}$ leads to conditions that involve the covariance tensor $\mathbf{C}_F^{(1)} = \langle (\mathbf{F} - \langle \mathbf{F} \rangle^{(1)}) \otimes (\mathbf{F} - \langle \mathbf{F} \rangle^{(1)}) \rangle^{(1)}$ of the deformation field in the matrix phase of the LCC, as outlined next.

Following Lopez-Pamies and Ponte Castañeda (2006a), $\mathbf{L}^{(1)}$ can be shown to be of the form:

$$L_{ijkl}^{(1)} = \bar{Q}_{rm} \bar{Q}_{jn} \bar{Q}_{sp} \bar{Q}_{lq} \bar{R}_{ir} \bar{R}_{ks} L_{mnpq}^*, \quad (18)$$

where indicial notation has been employed for clarity. In expression (18), $\bar{\mathbf{R}}$ is the macroscopic rotation tensor in the polar decomposition of $\bar{\mathbf{F}} = \bar{\mathbf{R}} \bar{\mathbf{U}}$, and $\bar{\mathbf{Q}}$ is the orthogonal tensor that characterizes the orientation of the macroscopic Lagrangian principal axes (i.e., the principal axes of $\bar{\mathbf{U}}$) via the relation $\bar{\mathbf{U}} = \bar{\mathbf{Q}} \bar{\mathbf{D}} \bar{\mathbf{Q}}^T$, where $\bar{\mathbf{D}} = \text{diag}(\bar{\lambda}_1, \bar{\lambda}_2, \bar{\lambda}_3)$ with respect to the laboratory frame of reference $\{\mathbf{e}_i\}$ and $\bar{\lambda}_i$ ($i = 1, 2, 3$) denote the principal stretches of $\bar{\mathbf{U}}$. Assuming now that \mathbf{L}^* is orthotropic with respect to $\{\mathbf{e}_i\}$ and possesses at most 9 independent components, denoted by ℓ_I^* ($I = 1, 2, \dots, 9$), the aforementioned optimization procedure for determining $\mathbf{L}^{(1)}$ leads to the following conditions:

$$(\hat{\mathbf{F}}^{(1)} - \bar{\mathbf{F}}) \cdot \frac{\partial \mathbf{L}^{(1)}}{\partial \ell_I^*} (\hat{\mathbf{F}}^{(1)} - \bar{\mathbf{F}}) = \frac{2}{1 - c_0} \frac{\partial \hat{W}_T}{\partial \ell_I^*} \quad (I = 1, 2, \dots, 9), \quad (19)$$

where it is recalled that the effective stored-energy function of the LCC \hat{W}_T is given by expression (13).

In summary, Eqs. (16), (17), and (19) constitute a system of 27 scalar, coupled, algebraic equations for the 27 scalar unknowns formed by the 9 components of $\hat{\mathbf{F}}^{(1)}$, the 9 components of $\bar{\mathbf{F}}^{(2)}$, and the 9 components of $\mathbf{L}^{(1)}$ (i.e., the 9 independent components ℓ_I^*). Having computed the values of all the components of $\hat{\mathbf{F}}^{(1)}$, $\bar{\mathbf{F}}^{(2)}$, and $\mathbf{L}^{(1)}$ for a given loading $\bar{\mathbf{F}}$, given stored-energy functions $\mathcal{W}^{(1)}$, $\mathcal{W}^{(2)}$, and given initial volume fraction c_0 , the values of the components of $\bar{\mathbf{F}}^{(1)}$ can be readily determined using relation (15). In turn, the second-order

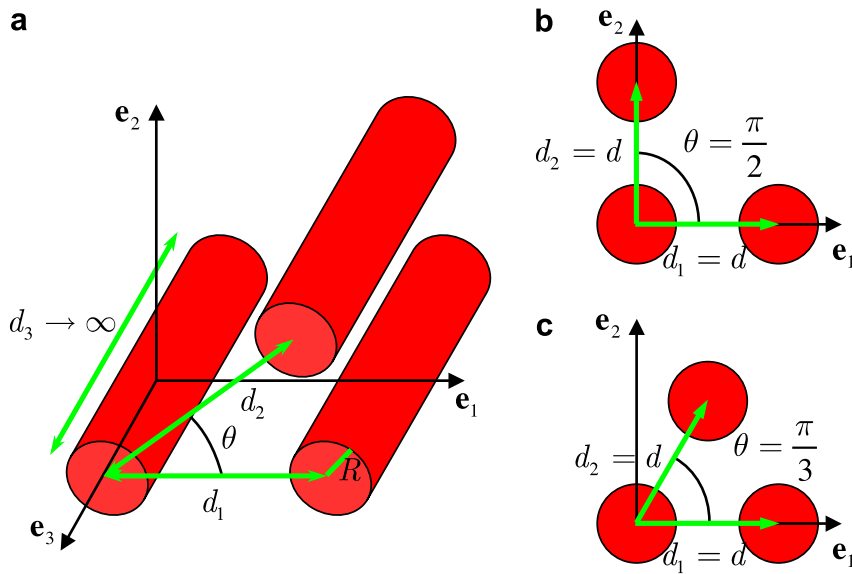


Fig. 1. Schematic representation of the microstructures of interest in this work in the undeformed configuration: (a) general, in-plane, periodic distribution, (b) square distribution, and (c) hexagonal distribution of circular fibers.

estimate for the effective stored-energy function \tilde{W} for fiber-reinforced elastomers can then be computed, from relation (14), using these results.

3.1. Estimates for the LCC

At this stage, the only variable that remains to be specified in the above formulation is the effective modulus tensor $\tilde{\mathbf{L}}$ of the LCC with the same microstructure as the actual hyperelastic composite. In view of the “particulate” type of microstructures of interest here, use is made in this work of the following Hashin–Shtrikman-type estimate for $\tilde{\mathbf{L}}$ due to Suquet (1990a) (see also Suquet, 1990b and Nemat-Nasser et al., 1982):

$$\tilde{\mathbf{L}} = \mathbf{L}^{(1)} + c_0 \left[(1 - c_0) \mathbf{P} - (\mathbf{L}^{(1)} - \mathbf{L}^{(2)})^{-1} \right]^{-1}, \tag{20}$$

where the microstructural tensor \mathbf{P} is given (in component form) by

$$P_{ijkl} = \frac{c_0}{1 - c_0} \sum_{\xi \in \mathcal{R}^* - \{0\}} N_{ik} \xi_j \xi_l \frac{4J_1^2(R|\xi|)}{R^2|\xi|^2} \tag{21}$$

with $\mathbf{N} = \mathbf{K}^{-1}$ and $K_{ik} = L_{imkn}^{(1)} \xi_m \xi_n$. In this expression, $J_1(\cdot)$ is the Bessel function of first kind, R is the initial radius³ of the fibers, and \mathcal{R}^* denotes the reciprocal lattice (i.e., in Fourier space) defining the periodic distribution of the fibers in the undeformed configuration (see, e.g., Kittel, 1968):

$$\mathcal{R}^* = \{ \xi | \xi = n_1 \mathbf{B}_1 + n_2 \mathbf{B}_2 + n_3 \mathbf{B}_3, \quad n_i \in \mathbb{Z} \} \tag{22}$$

with

$$\mathbf{B}_1 = 2\pi \frac{\mathbf{A}_2 \wedge \mathbf{A}_3}{\mathbf{A}_1 \cdot (\mathbf{A}_2 \wedge \mathbf{A}_3)}, \quad \mathbf{B}_2 = 2\pi \frac{\mathbf{A}_3 \wedge \mathbf{A}_1}{\mathbf{A}_1 \cdot (\mathbf{A}_2 \wedge \mathbf{A}_3)}, \quad \mathbf{B}_3 = 2\pi \frac{\mathbf{A}_1 \wedge \mathbf{A}_2}{\mathbf{A}_1 \cdot (\mathbf{A}_2 \wedge \mathbf{A}_3)}. \tag{23}$$

³ Of course, $|\xi|$ has dimensions of length⁻¹ so that the product $R|\xi|$ in (21) is dimensionless and can be ultimately written in terms of the volume fraction of the fibers c_0 .

Here, the base vectors \mathbf{A}_i ($i = 1, 2, 3$) characterize the periodic distribution of the fibers in the undeformed configuration in real space (i.e., in \mathbb{R}^3). Thus, choosing \mathbf{A}_3 to denote the fiber direction, we can conveniently write—without loss of generality:

$$\mathbf{A}_1 = d_1 \mathbf{e}_1, \quad \mathbf{A}_2 = d_2 (\cos \theta \mathbf{e}_1 + \sin \theta \mathbf{e}_2), \quad \mathbf{A}_3 = d_3 \mathbf{e}_3 \quad (24)$$

where it is recalled that the rectangular Cartesian basis $\{\mathbf{e}_i\}$ denotes the laboratory frame of reference,⁴ $d_3 \rightarrow \infty$, and d_1 , d_2 , and θ serve to describe the in-plane distribution of the fibers, as depicted by Fig. 1(a). In the sequel, for definiteness, we will restrict attention to square (see Fig. 1(b)) and hexagonal (see Fig. 1(c)) in-plane arrangement of fibers. For convenience, the specialization of expression (21) to these two cases is spelled out in Appendix A.

4. Overall behavior of periodic, fiber-reinforced elastomers

4.1. Constitutive hypotheses

The framework presented in the preceding sections is valid for any choice of the isotropic, elastomeric matrix phase, as well as for any choice of hyperelastic fibers. In what follows, for relative simplicity, we will restrict attention to matrix and fiber phases characterized by isotropic, stored-energy functions of the form:

$$W^{(r)}(\mathbf{F}) = \Phi^{(r)}(\lambda_1, \lambda_2, \lambda_3) = g^{(r)}(I) + h^{(r)}(J) + \frac{\kappa^{(r)}}{2} (J - 1)^2 \quad (25)$$

($r = 1, 2$), where $I \equiv I_1 = \text{tr} \mathbf{C} = \mathbf{F} \cdot \mathbf{F} = \lambda_1^2 + \lambda_2^2 + \lambda_3^2$, $J = \sqrt{\det \mathbf{C}} = \det \mathbf{F} = \lambda_1 \lambda_2 \lambda_3$ are, respectively, the first and third fundamental invariants of the right Cauchy–Green deformation tensor $\mathbf{C} = \mathbf{F}^T \mathbf{F}$, with λ_i ($i = 1, 2, 3$) denoting the principal stretches associated with \mathbf{F} . Further, $\kappa^{(r)}$ denotes the bulk modulus at zero strain of phase r , and $g^{(r)}$ and $h^{(r)}$ are twice-differentiable material functions that satisfy the following relations: $g^{(r)}(3) = h^{(r)}(1) = 0$, $g_I^{(r)}(3) = \mu^{(r)}/2$, $h_J^{(r)}(1) = -\mu^{(r)}$, and $4g_{II}^{(r)}(3) + h_{JJ}^{(r)}(1) = \mu^{(r)}/3$. Here, $\mu^{(r)}$ denotes the shear modulus at zero strain of phase r , and the subscripts I and J indicate differentiation with respect to these invariants. Note that when the above conditions are satisfied, the stored-energy function (25) linearizes properly, in the sense that $W^{(r)}(\mathbf{F}) = (1/2) (\kappa^{(r)} - 2/3\mu^{(r)}) (\text{tr} \boldsymbol{\varepsilon})^2 + \mu^{(r)} \text{tr} \boldsymbol{\varepsilon}^2 + o(\boldsymbol{\varepsilon}^3)$, where $\boldsymbol{\varepsilon}$ is the infinitesimal strain tensor, as $\mathbf{F} \rightarrow \mathbf{I}$. Furthermore, note that to recover incompressible behavior in (25), it suffices to make the parameter $\kappa^{(r)}$ tend to infinity (in which case $W^{(r)}(\mathbf{F}) = g^{(r)}(I)$ together with the incompressibility constraint $J = 1$).

Within the context of the material model (25), it is worth noticing that by requiring $g^{(r)}(I)$ and $h^{(r)}(J) + \frac{\kappa^{(r)}}{2} (J - 1)^2$ to be strictly convex functions of their arguments, the stored-energy function (25) is strongly elliptic. This constitutive hypothesis, which will be adopted here, guarantees that no localized deformations will develop within the given elastomeric matrix and fiber phases, in accord with experimental evidence for “neat” rubber-like solids. Note also that the stored-energy function (25) is an extension of the so-called generalized Neo-Hookean (or I_1 -based) materials to account for compressibility that includes constitutive models widely used in the literature. The analysis that follows will be carried out for stored-energy functions of the general form (25). However, for definiteness, specific results will be presented and discussed for fiber-reinforced elastomers with Gent (Gent, 1996) matrix and fiber phases:

$$W^{(r)}(\mathbf{F}) = -\frac{J_m^{(r)} \mu^{(r)}}{2} \ln \left[1 - \frac{I - 3}{J_m^{(r)}} \right] - \mu^{(r)} \ln J + \left(\frac{\kappa^{(r)}}{2} - \frac{J_m^{(r)} + 3}{3J_m^{(r)}} \mu^{(r)} \right) (J - 1)^2. \quad (26)$$

In this material model, the parameter $J_m^{(r)}$ indicates the limiting value for $I - 3$ at which the elastomer locks up. Note that the stored-energy function (26) is strongly elliptic for all deformations provided that $\mu^{(r)} > 0$, $J_m^{(r)} > 0$, and $\kappa^{(r)} > 2\mu^{(r)}/J_m^{(r)} + 2/3\mu^{(r)}$, which will be assumed here. Note further that upon taking the limit $J_m^{(r)} \rightarrow \infty$ in (26), the Gent material reduces to a compressible Neo-Hookean solid.

⁴ Subsequently, unless otherwise indicated, the components of all tensorial quantities will be written with respect to $\{\mathbf{e}_i\}$.

4.2. Voigt bound

Before proceeding with the computation of the second-order estimate, it proves useful, for comparison purposes, to recall the Voigt upper bound (Ogden, 1978) for hyperelastic composites. Thus, when specialized to fiber-reinforced elastomers with initial volume fraction of fibers c_0 and (matrix and fiber) phases of the form (25), this rigorous upper bound leads to:

$$\hat{W}(\bar{\mathbf{F}}) = (1 - c_0)[g^{(1)}(\bar{I}) + h^{(1)}(\bar{J})] + c_0[g^{(2)}(\bar{I}) + h^{(2)}(\bar{J})] + \frac{(1 - c_0)\kappa^{(1)} + c_0\kappa^{(2)}}{2}(\bar{J} - 1)^2, \tag{27}$$

where $\bar{I} = \bar{\mathbf{F}} \cdot \bar{\mathbf{F}} = \bar{\lambda}_1^2 + \bar{\lambda}_2^2 + \bar{\lambda}_3^2$ and $\bar{J} = \det \bar{\mathbf{F}} = \bar{\lambda}_1 \bar{\lambda}_2 \bar{\lambda}_3$ stand for, respectively, the first and third invariants associated with the macroscopic deformation gradient tensor $\bar{\mathbf{F}}$. Note that the bound (27) depends only on the initial volume fraction of the fibers, c_0 , and contains no dependence on higher-order statistical information about the microstructure. This limitation can be readily recognized in the present context from the fact that the stored-energy function (27) is isotropic, while the exact overall behavior of the fiber-reinforced elastomers of interest in this work is obviously orthotropic. Moreover, it is interesting to remark that the Voigt bound (27) remains strongly elliptic for all deformations $\bar{\mathbf{F}}$, provided that $g^{(r)}(\bar{I})$ and $h^{(r)}(\bar{J}) + \frac{\kappa^{(r)}}{2}(\bar{J} - 1)^2$ ($r = 1, 2$) are strictly convex functions of their arguments, which has been assumed here.

4.3. Second-order homogenization estimates

In this subsection, we spell out the main steps in the computation of the second-order estimate (14) for the effective stored-energy function \hat{W} of elastomers, characterized by stored-energy functions of the form (25), reinforced with monodisperse, initially circular, aligned cylindrical fibers—also characterized by potentials of the form (25)—distributed periodically in: (a) square and (b) hexagonal arrangements in the undeformed configuration, as depicted in Fig. 2.

In order to carry out the computation for the second-order estimate (14) for the above-specified class of elastomeric composites, the precise form of the modulus tensor \mathbf{L}^* , introduced in expression (18), needs to be spelled out. In this regard, recall first that \mathbf{L}^* is orthotropic with respect to the laboratory frame of reference $\{\mathbf{e}_i\}$ and has at most 9 independent components, which are termed ℓ_i^* . In this work, for simplicity, we introduce further constraints among the components of \mathbf{L}^* in order to reduce them to 7 independent components. Thus, following Lopez-Pamies and Ponte Castañeda (in press-a), the independent principal components of \mathbf{L}^* are chosen to be $L_{1111}^* = \ell_1^*$, $L_{2222}^* = \ell_2^*$, $L_{3333}^* = \ell_3^*$, $L_{1122}^* = \ell_4^*$, $L_{1133}^* = \ell_5^*$, $L_{2233}^* = \ell_6^*$, $L_{1212}^* = \ell_7^*$, while the other non-zero components

$$\begin{aligned} L_{2121}^* &= L_{1313}^* = L_{3131}^* = L_{2323}^* = L_{3232}^* = \ell_7^*, \\ L_{1221}^* &= \sqrt{(\ell_1^* - \ell_7^*)(\ell_2^* - \ell_7^*)} - \ell_4^*, \\ L_{1331}^* &= \sqrt{(\ell_1^* - \ell_7^*)(\ell_3^* - \ell_7^*)} - \ell_5^*, \\ L_{2332}^* &= \sqrt{(\ell_2^* - \ell_7^*)(\ell_3^* - \ell_7^*)} - \ell_6^*, \end{aligned} \tag{28}$$

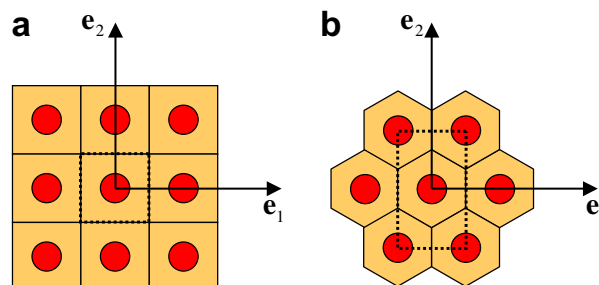


Fig. 2. Undeformed configuration depiction of: (a) periodic square and (b) periodic hexagonal arrangement of circular fibers.

are dependent. The motivation for the constraints (28) is twofold: (i) relations (28) are consistent with the tangent modulus of Neo-Hookean materials;⁵ and (ii) conditions (28) simplify considerably the computations involved. It should be emphasized, however, that other choices are possible in principle.

Having specified the functional form of \mathbf{L}^* , and hence that of $\mathbf{L}^{(1)}$ via (18), we proceed next to compute the variable $\hat{\mathbf{F}}^{(1)}$, needed in the computation of the second-order estimate (14) for \hat{W} . Thus, by making use of the prescribed form for \mathbf{L}^* , together with expression (20) for the Suquet estimate for $\hat{\mathbf{L}}$, equations (19) can be seen to reduce to 7 nonlinear, algebraic equations for 7 combinations of the components of $\hat{\mathbf{F}}^{(1)}$. These equations—as it will become more clear further below—are more conveniently expressed in terms of the variable \mathbf{Y} :

$$\mathbf{Y} = \overline{\mathbf{Q}}^T \overline{\mathbf{R}}^T (\hat{\mathbf{F}}^{(1)} - \overline{\mathbf{F}}) \overline{\mathbf{Q}} \quad (29)$$

which leads to the expressions:

$$\begin{aligned} Y_{11}^2 + 2f_1 Y_{12} Y_{21} + 2f_2 Y_{13} Y_{31} &= \frac{2}{1-c_0} \frac{\partial \hat{W}_T}{\partial \ell_1^*} \doteq k_1, \\ Y_{22}^2 + \frac{1}{2f_1} Y_{12} Y_{21} + 2f_3 Y_{23} Y_{32} &= \frac{2}{1-c_0} \frac{\partial \hat{W}_T}{\partial \ell_2^*} \doteq k_2, \\ Y_{33}^2 + \frac{1}{2f_2} Y_{13} Y_{31} + \frac{1}{2f_3} Y_{23} Y_{32} &= \frac{2}{1-c_0} \frac{\partial \hat{W}_T}{\partial \ell_3^*} \doteq k_3, \\ Y_{11} Y_{22} - Y_{12} Y_{21} &= \frac{1}{1-c_0} \frac{\partial \hat{W}_T}{\partial \ell_4^*} \doteq \frac{k_4}{2}, \\ Y_{11} Y_{33} - Y_{13} Y_{31} &= \frac{1}{1-c_0} \frac{\partial \hat{W}_T}{\partial \ell_5^*} \doteq \frac{k_5}{2}, \\ Y_{22} Y_{33} - Y_{23} Y_{32} &= \frac{1}{1-c_0} \frac{\partial \hat{W}_T}{\partial \ell_6^*} \doteq \frac{k_6}{2}, \end{aligned} \quad (30)$$

$$Y_{12}^2 + Y_{21}^2 + Y_{13}^2 + Y_{31}^2 + Y_{23}^2 + Y_{32}^2 + 2f_4 Y_{12} Y_{21} + 2f_5 Y_{13} Y_{31} + 2f_6 Y_{23} Y_{32} = \frac{2}{1-c_0} \frac{\partial \hat{W}_T}{\partial \ell_7^*} \doteq k_7.$$

Here, $f_1 = \partial L_{1221}^* / \partial \ell_1^*$, $f_2 = \partial L_{1331}^* / \partial \ell_1^*$, $f_3 = \partial L_{2332}^* / \partial \ell_2^*$, $f_4 = \partial L_{1221}^* / \partial \ell_7^*$, $f_5 = \partial L_{1331}^* / \partial \ell_7^*$, $f_6 = \partial L_{2332}^* / \partial \ell_7^*$, and

$$k_I = -\frac{c_0}{(1-c_0)} (\overline{\mathbf{F}} - \overline{\mathbf{F}}^{(2)}) \cdot \frac{\partial \mathbf{L}^{(1)}}{\partial \ell_I^*} (\overline{\mathbf{F}} - \overline{\mathbf{F}}^{(2)}) - c_0 \mathbf{E} \cdot \frac{\partial \mathbf{P}}{\partial \ell_I^*} \mathbf{E} \quad (31)$$

($I = 1, 2, \dots, 7$), where $\mathbf{E} = \mathbf{L}^{(1)}(\overline{\mathbf{F}} - \overline{\mathbf{F}}^{(2)}) - \mathcal{S}^{(1)}(\overline{\mathbf{F}}) + \mathcal{S}^{(2)}(\overline{\mathbf{F}}^{(2)})$ has been introduced for convenience, and it is recalled that the explicit expressions for the tensor \mathbf{P} for the two types of periodic microstructures considered here are given in Appendix A. It is not difficult to check that—though nonlinear—equations (30) may be solved *explicitly* to yield two distinct solutions for Y_{11} , Y_{22} , Y_{33} in terms of which the combinations $p_1 \doteq Y_{12} Y_{21}$, $p_2 \doteq Y_{13} Y_{31}$, $p_3 \doteq Y_{23} Y_{32}$, and $s \doteq Y_{12}^2 + Y_{21}^2 + Y_{13}^2 + Y_{31}^2 + Y_{23}^2 + Y_{32}^2$ may be uniquely determined. The two solutions for Y_{11} , Y_{22} , and Y_{33} are as follows:

$$\begin{aligned} Y_{11} &= \pm \frac{(k_1 + f_1 k_4 + f_2 k_5) \sqrt{C_1 C_2}}{C_2 \sqrt{C_3}}, \\ Y_{22} &= \pm \frac{(k_2 + 4f_1(k_2 + f_3 k_6)) C_2}{2\sqrt{C_1 C_2} \sqrt{C_3}}, \\ Y_{33} &= \pm \frac{(f_3 k_5 + f_2(4f_3 k_3 + k_6)) \sqrt{C_3}}{\sqrt{C_1 C_2}} \end{aligned} \quad (32)$$

with $C_1 = f_2(4f_1 k_2 + k_4) + 4f_1 f_3^2(4f_2 k_3 + k_5) + 2f_3(k_1 + f_1 k_4 + f_2 k_5 + 4f_1 f_2 k_6)$, $C_2 = f_2(4f_1 k_2 + k_4 + 2f_2 k_6) + 2f_3(k_1 + f_1 k_4 + 2f_2(2f_2 k_3 + k_5 + f_1 k_6))$, $C_3 = k_1 + f_2 k_5 + 2f_1(4f_2 f_3 k_3 + k_4 + f_3 k_5 + f_2 k_6) + 4f_1^2(k_2 + f_3 k_6)$,

⁵ In fact, conditions (28)₁ are consistent with tangent moduli of any isotropic stored-energy function of the general form (25).

where it must be emphasized that the positive (and negative) signs must be chosen to go together in the roots for Y_{11} , Y_{22} , and Y_{33} . The corresponding final expressions for the remaining combinations read as:

$$p_1 = Y_{11}Y_{22} - k_4/2, \quad p_2 = Y_{11}Y_{33} - k_5/2, \quad p_3 = Y_{22}Y_{33} - k_6/2, \quad \text{and} \\ s = k_7 - 2(f_4p_1 + f_5p_2 + f_6p_3). \tag{33}$$

At this point, it is expedient to make a few remarks regarding expressions (32) and (33). First, it is important to emphasize that these relations provide *explicit* expressions for 7 combinations of the components of $\hat{\mathbf{F}}^{(1)}$ in terms of the applied loading $\bar{\mathbf{F}}$, the constitutive functions $g^{(r)}$, $h^{(r)}$, $\kappa^{(r)}$ ($r = 1, 2$), the initial volume fraction of fibers c_0 , as well as the moduli ℓ_I^* ($I = 1, 2, \dots, 7$) and the phase average deformation gradient in the fiber phase of the linear comparison composite $\bar{\mathbf{F}}^{(2)}$. Note, however, that the tensorial variable $\hat{\mathbf{F}}^{(1)}$ has 9 components, so that two more relations are required to entirely characterize $\hat{\mathbf{F}}^{(1)}$, as discussed below.

Next, making use of each of the two distinct roots (32) for the combinations Y_{11} , Y_{22} , Y_{33} , p_1 , p_2 , p_3 , s in the generalized secant condition (17) can be shown to lead to a system of 9 scalar equations for the 9 unknowns constituted by the 2 combinations of $\hat{\mathbf{F}}^{(1)}$: $p_4 = Y_{23}Y_{31}Y_{12}$, $p_5 = Y_{32}Y_{13}Y_{21}$, and the 7 moduli ℓ_I^* . From algebraic manipulation of the resulting system, it can be seen that one such equation is satisfied trivially, and the remaining 8 equations may be cast in the following expedient manner:

$$\begin{aligned} \ell_1^*Y_{11} + \ell_4^*Y_{22} + \ell_5^*Y_{33} &= 2\hat{g}_I^{(1)}(Y_{11} + \bar{\lambda}_1) + \left[\hat{h}_J^{(1)} + \kappa^{(1)}(\hat{J}^{(1)} - 1)\right] \\ &\times ((Y_{22} + \bar{\lambda}_2)(Y_{33} + \bar{\lambda}_3) - p_3) - 2\bar{g}_I^{(1)}\bar{\lambda}_1 - \left(\bar{h}_J^{(1)} + \kappa^{(1)}(\bar{J} - 1)\right)\bar{\lambda}_2\bar{\lambda}_3, \\ \ell_4^*Y_{11} + \ell_2^*Y_{22} + \ell_6^*Y_{33} &= 2\hat{g}_I^{(1)}(Y_{22} + \bar{\lambda}_2) + \left[\hat{h}_J^{(1)} + \kappa^{(1)}(\hat{J}^{(1)} - 1)\right] \\ &\times ((Y_{11} + \bar{\lambda}_1)(Y_{33} + \bar{\lambda}_3) - p_2) - 2\bar{g}_I^{(1)}\bar{\lambda}_2 - \left(\bar{h}_J^{(1)} + \kappa^{(1)}(\bar{J} - 1)\right)\bar{\lambda}_1\bar{\lambda}_3, \\ \ell_5^*Y_{11} + \ell_6^*Y_{22} + \ell_3^*Y_{33} &= 2\hat{g}_I^{(1)}(Y_{33} + \bar{\lambda}_3) + \left[\hat{h}_J^{(1)} + \kappa^{(1)}(\hat{J}^{(1)} - 1)\right] \\ &\times ((Y_{11} + \bar{\lambda}_1)(Y_{22} + \bar{\lambda}_2) - p_1) - 2\bar{g}_I^{(1)}\bar{\lambda}_3 - \left(\bar{h}_J^{(1)} + \kappa^{(1)}(\bar{J} - 1)\right)\bar{\lambda}_1\bar{\lambda}_2, \\ L_{1221}^*p_1 &= \left[\hat{h}_J^{(1)} + \kappa^{(1)}(\hat{J}^{(1)} - 1)\right](p_4 - p_1(Y_{33} + \bar{\lambda}_3)), \\ L_{1331}^*p_2 &= \left[\hat{h}_J^{(1)} + \kappa^{(1)}(\hat{J}^{(1)} - 1)\right](p_4 - p_2(Y_{22} + \bar{\lambda}_2)), \\ L_{2332}^*p_3 &= \left[\hat{h}_J^{(1)} + \kappa^{(1)}(\hat{J}^{(1)} - 1)\right](p_4 - p_3(Y_{11} + \bar{\lambda}_1)), \\ \ell_7^* &= 2\hat{g}_I^{(1)}, \end{aligned} \tag{34}$$

and

$$p_4 = p_5, \tag{35}$$

where $\bar{g}^{(1)} = g^{(1)}(\bar{I})$, $\bar{h}^{(1)} = h^{(1)}(\bar{J})$, $\hat{g}_I^{(1)} = g_I^{(1)}(\hat{I}^{(1)})$, $\hat{h}_J^{(1)} = h_J^{(1)}(\hat{J}^{(1)})$ have been introduced for ease of notation, with

$$\hat{J}^{(1)} = \hat{\mathbf{F}}^{(1)} \cdot \hat{\mathbf{F}}^{(1)} = (\mathbf{Y} + \bar{\mathbf{D}}) \cdot (\mathbf{Y} + \bar{\mathbf{D}}) = (Y_{11} + \bar{\lambda}_1)^2 + (Y_{22} + \bar{\lambda}_2)^2 + (Y_{33} + \bar{\lambda}_3)^2 + s, \tag{36}$$

$$\begin{aligned} \hat{J}^{(1)} = \det \hat{\mathbf{F}}^{(1)} = \det(\mathbf{Y} + \bar{\mathbf{D}}) &= (Y_{11} + \bar{\lambda}_1)(Y_{22} + \bar{\lambda}_2)(Y_{33} + \bar{\lambda}_3) \\ &- p_1(Y_{33} + \bar{\lambda}_3) - p_2(Y_{22} + \bar{\lambda}_2) - p_3(Y_{11} + \bar{\lambda}_1) + 2p_4. \end{aligned} \tag{37}$$

A direct implication of the fact that one of the generalized secant equations (17) is satisfied trivially is that the components of $\hat{\mathbf{F}}^{(1)}$ enter the above framework exclusively through 8—as opposed to 9—distinct combinations, namely: Y_{11} , Y_{22} , Y_{33} , p_1 , p_2 , p_3 , p_4 , and s . As described below, these are the only combinations needed in the computation of the second-order estimate (14) for \hat{W} . Having clarified this point, we remark next that—by recalling the definitions $p_1 = Y_{12}Y_{21}$, $p_2 = Y_{13}Y_{31}$, $p_3 = Y_{23}Y_{32}$, $p_4 = Y_{23}Y_{31}Y_{12}$, and $p_5 = Y_{32}Y_{13}Y_{21}$ —Eq. (35) can be solved in closed form to render:

$$p_4 = \pm \sqrt{p_1 p_2 p_3}. \quad (38)$$

Now, each of the two roots in (38) can be substituted back in (34) to generate a system of 7 equations for the 7 moduli ℓ_i^* . Note that—since \mathbf{Y} depends directly on $\bar{\mathbf{F}}^{(2)}$ —the resulting equations depend directly on the variable $\bar{\mathbf{F}}^{(2)}$, which must be determined from Eq. (16). In this connection, it is helpful to note that by making use of the expression (20) for the Suquet estimate for $\bar{\mathbf{L}}$, Eq. (16) can be simplified substantially (see Lopez-Pamies and Ponte Castañeda, 2006a for details) and recast as follows:

$$\bar{\mathbf{F}}^{(2)} = \bar{\mathbf{F}} + (1 - c_0) \mathbf{P} [\mathcal{S}^{(1)}(\bar{\mathbf{F}}) - \mathcal{S}^{(2)}(\bar{\mathbf{F}}^{(2)}) - \mathbf{L}^{(1)}(\bar{\mathbf{F}} - \bar{\mathbf{F}}^{(2)})]. \quad (39)$$

In short, relations (34) and (39) are seen to constitute a closed system of $(7 + 9 =) 16$ scalar, coupled, algebraic equations for the 16 scalar unknowns formed by the 7 moduli ℓ_i^* and the 9 components of $\bar{\mathbf{F}}^{(2)}$. In general, these equations must be solved numerically.

Having computed from (34) and (39) the values of the 7 independent components of $\mathbf{L}^{(1)}$ (i.e., ℓ_i^*) and the 9 components of $\bar{\mathbf{F}}^{(2)}$ for a given loading, $\bar{\mathbf{F}}$, given matrix and fiber behavior, $g^{(r)}, h^{(r)}, \kappa^{(r)}$ ($r = 1, 2$), and given initial volume fraction of fibers, c_0 , the values of the components of $\bar{\mathbf{F}}^{(1)}$ and the relevant combinations of $\check{\mathbf{F}}^{(1)}$ (i.e., $Y_{11}, Y_{22}, Y_{33}, p_1, p_2, p_3, s, p_4$) may be readily determined using relations (15), (32), (33), and (38). In turn, these results can be used to compute the second-order estimate (14) for the effective stored-energy function \hat{W} of fiber-reinforced elastomers. The final expression for \hat{W} may be written as follows:

$$\begin{aligned} \hat{W}(\bar{\mathbf{F}}) = & (1 - c_0) \left[g^{(1)}(\hat{J}^{(1)}) + h^{(1)}(\hat{J}^{(1)}) + \frac{\kappa^{(1)}}{2}(\hat{J}^{(1)} - 1)^2 \right] \\ & + c_0 \left[g^{(2)}(\bar{J}^{(2)}) + h^{(2)}(\bar{J}^{(2)}) + \frac{\kappa^{(2)}}{2}(\bar{J}^{(2)} - 1)^2 \right] - (1 - c_0) \mathcal{S}^{(1)}(\bar{\mathbf{D}}) \cdot (\mathbf{Y} - \check{\mathbf{F}}^{(1)}), \end{aligned} \quad (40)$$

where $\check{\mathbf{F}}^{(1)} = \bar{\mathbf{Q}}^T \bar{\mathbf{R}}^T (\bar{\mathbf{F}}^{(1)} - \bar{\mathbf{F}}) \bar{\mathbf{Q}}$, and $\bar{J}^{(2)} = \bar{\mathbf{F}}^{(2)} \cdot \bar{\mathbf{F}}^{(2)}$ and $\bar{J}^{(2)} = \det \bar{\mathbf{F}}^{(2)}$ have been introduced for convenience.

We conclude this subsection by making the following three practical remarks. First, it is important to emphasize that the second-order estimate (40) can be shown to be *objective* and *orthotropic*, in accord with the appropriate *exact* result (9). Second, it should be noted that the effective stored-energy function (40) does indeed depend—as pointed out above—on the variable $\check{\mathbf{F}}^{(1)}$ only through the 8 combinations $Y_{11}, Y_{22}, Y_{33}, p_1, p_2, p_3, p_4$, and s . Moreover, it is important to point out that there are 4 possible combinations of the roots introduced in (32) and (38), which lead to 4 different estimates for \hat{W} . In the case when the bulk moduli (at zero strain) of the matrix and fibers, $\kappa^{(1)}$ and $\kappa^{(2)}$, are of the order of the shear moduli (at zero strain), $\mu^{(1)}$ and $\mu^{(2)}$, all 4 root combinations lead to very similar results for the effective stored-energy function \hat{W} . However, when the bulk moduli are significantly larger than the shear moduli—namely, when the composite is nearly incompressible—the estimates produced by the 4 distinct combinations are very different. In fact, in this case, it can be shown that only one root combination generates physically meaningful estimates relative to the other 3 possibilities. More precisely, for $\kappa^{(r)} \gg \mu^{(s)}$ ($r, s = 1, 2$), the “negative” (–) root in (32), together with the choice $p_4 = \text{sign} \left(\check{F}_{11}^{(1)} \check{F}_{22}^{(1)} \check{F}_{33}^{(1)} \right) \sqrt{p_1 p_2 p_3}$ in (35) leads to estimates that are superior to the other 3 alternatives. Given that rubber-like materials are (in general) fairly incompressible, this is the root combination that should be selected to compute the second-order estimate (40) for fiber-reinforced elastomers.

4.3.1. Generalized plane-strain loading

The second-order estimate (40) is valid for general macroscopic deformations $\bar{\mathbf{F}}$. In the following section, we will be particularly interested in *generalized plane-strain* macroscopic deformations of the form:

$$\bar{\mathbf{F}} = \bar{F}_{11} \mathbf{e}_1 \otimes \mathbf{e}_1 + \bar{F}_{12} \mathbf{e}_1 \otimes \mathbf{e}_2 + \bar{F}_{21} \mathbf{e}_2 \otimes \mathbf{e}_1 + \bar{F}_{22} \mathbf{e}_2 \otimes \mathbf{e}_2 + \bar{\lambda}_3 \mathbf{e}_3 \otimes \mathbf{e}_3. \quad (41)$$

For this type of loading conditions, the computation of (40) simplifies substantially. More specifically, for macroscopic loadings of the form (41), it is easy to check that 5 out of the 9 scalar equations in (39) are satisfied identically by the choices:

$$\bar{F}_{33}^{(2)} = \bar{\lambda}_3 \quad \text{and} \quad \bar{F}_{13}^{(2)} = \bar{F}_{31}^{(2)} = \bar{F}_{23}^{(2)} = \bar{F}_{32}^{(2)} = 0, \quad (42)$$

while the remaining 4 equations for the 4 in-plane components $\bar{F}_{11}^{(2)}, \bar{F}_{22}^{(2)}, \bar{F}_{12}^{(2)}, \bar{F}_{21}^{(2)}$ are given by:

$$\bar{F}_{\alpha\beta}^{(2)} = \bar{F}_{\alpha\beta} + (1 - c_0)P_{\alpha\beta\gamma\delta} \left[\mathcal{S}_{\gamma\delta}^{(1)}(\bar{\mathbf{F}}) - \mathcal{S}_{\gamma\delta}^{(2)}(\bar{\mathbf{F}}^{(2)}) - L_{\gamma\delta\zeta\eta}^{(1)}(\bar{F}_{\zeta\eta} - \bar{F}_{\zeta\eta}^{(2)}) \right]. \tag{43}$$

Here, Greek indices range from 1 to 2, and it is important to note, for later use, that Eqs. (43) depend on \mathbf{L}^* only through the moduli ℓ_1^* , ℓ_2^* , ℓ_4^* , and ℓ_7^* .

Next, under conditions (41), $k_3 = k_5 = k_6 = 0$ in (31), so that expressions (32), (33), and (38) reduce to:

$$Y_{11} = \pm \frac{k_1 + 2f_1k_4}{\sqrt{k_1 + 4f_1(f_1k_2 + k_4)}}, \quad Y_{22} = \pm \frac{2f_1k_2 + k_4}{\sqrt{k_1 + 4f_1(f_1k_2 + k_4)}}, \quad Y_{33} = 0, \tag{44}$$

and

$$p_1 = Y_{11}Y_{22} - k_4/2, \quad s = k_7 - 2f_4p_1, \quad p_2 = p_3 = p_4 = 0. \tag{45}$$

Note that—similar to Eqs. (43)—expressions (44) and (45) also depend on \mathbf{L}^* only through the moduli ℓ_1^* , ℓ_2^* , ℓ_4^* , and ℓ_7^* .

Finally, making use of the above simplifications, it is straightforward to see that 2 out of the 7 scalar equations in (34) are satisfied trivially, while the remaining 5 nontrivial equations reduce to:

$$\begin{aligned} \ell_1^*Y_{11} + \ell_4^*Y_{22} &= 2\hat{g}_I^{(1)}(Y_{11} + \bar{\lambda}_1) + \left[\hat{h}_J^{(1)} + \kappa^{(1)}(\hat{J}^{(1)} - 1) \right] (Y_{22} + \bar{\lambda}_2)\bar{\lambda}_3 \\ &\quad - 2\bar{g}_I^{(1)}\bar{\lambda}_1 - \left[\bar{h}_J^{(1)} + \kappa^{(1)}(\bar{J} - 1) \right] \bar{\lambda}_2\bar{\lambda}_3, \\ \ell_4^*Y_{11} + \ell_2^*Y_{22} &= 2\hat{g}_I^{(1)}(Y_{22} + \bar{\lambda}_2) + \left[\hat{h}_J^{(1)} + \kappa^{(1)}(\hat{J}^{(1)} - 1) \right] (Y_{11} + \bar{\lambda}_1)\bar{\lambda}_3 \\ &\quad - 2\bar{g}_I^{(1)}\bar{\lambda}_2 - \left[\bar{h}_J^{(1)} + \kappa^{(1)}(\bar{J} - 1) \right] \bar{\lambda}_1\bar{\lambda}_3, \\ L_{1221}^* &= - \left[\hat{h}_J^{(1)} + \kappa^{(1)}(\hat{J}^{(1)} - 1) \right] \bar{\lambda}_3, \\ \ell_7^* &= 2\hat{g}_I^{(1)}, \end{aligned} \tag{46}$$

and

$$\begin{aligned} \ell_5^*Y_{11} + \ell_6^*Y_{22} &= 2\hat{g}_I^{(1)}\bar{\lambda}_3 + \left[\hat{h}_J^{(1)} + \kappa^{(1)}(\hat{J}^{(1)} - 1) \right] \times ((Y_{11} + \bar{\lambda}_1)(Y_{22} + \bar{\lambda}_2) - p_1) - 2\bar{g}_I^{(1)}\bar{\lambda}_3 \\ &\quad - \left(\bar{h}_J^{(1)} + \kappa^{(1)}(\bar{J} - 1) \right) \bar{\lambda}_1\bar{\lambda}_2. \end{aligned} \tag{47}$$

To summarize, relations (43) and (46) constitute a *closed* system of 8 coupled, algebraic equations for the 4 in-plane components $\bar{F}_{11}^{(2)}$, $\bar{F}_{22}^{(2)}$, $\bar{F}_{12}^{(2)}$, $\bar{F}_{21}^{(2)}$ and the 4 moduli ℓ_1^* , ℓ_2^* , ℓ_4^* , and ℓ_7^* . Knowledge of these variables, together with the explicit relations (42), (44), (45), suffices to compute the second-order estimate (40) for \hat{W} for generalized plane-strain deformations (41). As a final remark, it is interesting to note that Eq. (47), which establishes a connection between the moduli ℓ_5^* , ℓ_6^* and the in-plane variables $\bar{F}_{11}^{(2)}$, $\bar{F}_{22}^{(2)}$, $\bar{F}_{12}^{(2)}$, $\bar{F}_{21}^{(2)}$, ℓ_1^* , ℓ_2^* , ℓ_4^* , and ℓ_7^* , does not intervene in the computation of \hat{W} .

5. Results and discussion

In this section, the second-order estimate (40) is used to study the effective stress–strain response and the macroscopic stability of Gent elastomers reinforced with monodisperse, initially circular, cylindrical Gent fibers aligned in the \mathbf{e}_3 axis and distributed periodically with square (*SA*) and hexagonal (*HA*) arrangements in the \mathbf{e}_1 – \mathbf{e}_2 plane in the undeformed configuration (see Fig. 2). Results are given for compressible (matrix and fiber) phases with lock-up parameters $J_m^{(1)} = J_m^{(2)} = J_m = 100$, and are computed up to the point at which either the effective incremental modulus, $\hat{\mathcal{L}} = \partial^2 \hat{W} / \partial \bar{\mathbf{F}}^2$, is found to lose strong ellipticity—according to condition (10)—or fiber contact is detected. (The interested reader is referred to Chapter 2 of Lopez-Pamies (2006) for details on the estimation of fiber-contact within the Suquet approximation (20) for the LCC.) If neither of these phenomena occurs, the results are truncated at some sufficiently large value of the deformation. For clarity, the points at which the homogenized material loses strong ellipticity are denoted with the symbol “○” in the figures, whereas the symbol “●” is utilized to indicate contact between fibers.

The results presented in this section are organized as follows. First, we present and discuss the response of fiber-reinforced elastomers subjected to *axisymmetric shear*. These results are followed by the effective response of fiber-reinforced elastomers subjected to *in-plane pure* and *simple shear*. We finish this section by providing results for *out-of-plane pure shear*. The motivation behind the selection of these results is to provide an overall understanding of the effective response of fiber-reinforced elastomers under out-of-plane, in-plane, and coupled in-plane and out-of-plane modes of deformation, while illustrating the intimate connection between the effective behavior and macroscopic stability of these materials with the evolution of the underlying microstructure.

5.1. Axisymmetric shear

Figs. 3 and 4 present the effective behavior, as predicted by the second-order estimate (40) (denoted by SOE in the plots) and the Voigt bound (27), for a compressible Gent matrix reinforced with an initially periodic hexagonal distribution (HA) of Gent fibers under axisymmetric shear deformation: $\bar{\mathbf{F}} = \bar{\lambda}_1 \mathbf{e}_1 \otimes \mathbf{e}_1 + \bar{\lambda}_2 \mathbf{e}_2 \otimes \mathbf{e}_2 + \bar{\lambda}_3 \mathbf{e}_3 \otimes \mathbf{e}_3$ with $\bar{\lambda}_3 = \bar{\lambda}$ and $\bar{\lambda}_1 = \bar{\lambda}_2 = \bar{\lambda}^{-1/2}$. Fig. 3 illustrates results for tension in the fiber direction (i.e., $\bar{\lambda} \geq 1$) and Fig. 4, for compression (i.e., $\bar{\lambda} \leq 1$). In particular, results are shown for compressibility ratios $\kappa^{(1)}/\mu^{(1)} = \kappa^{(2)}/\mu^{(2)} = 50$, shear contrast $t = \mu^{(2)}/\mu^{(1)} = 20$, and initial volume fractions of fibers $c_0 = 15, 25$ and 35% , as a function of the logarithmic strain $\bar{e} = \ln \bar{\lambda}$. Parts (a) show the normalized effective stored-energy function $\hat{W}/\mu^{(1)}$, and parts (b), the normalized stress in the fiber direction $\bar{S}_{33}/\mu^{(1)} = (1/\mu^{(1)})\partial\hat{W}/\partial\bar{F}_{33}$.

It is observed from both figures, Figs. 3 and 4, that the effective behavior of the fiber-reinforced elastomer is stiffer for higher values of the initial volume fraction of fibers c_0 , as expected on physical grounds. In this connection, note that the behavior of the composite (i.e., $c_0 > 0$) is much stiffer than that of the matrix material (i.e., $c_0 = 0$). Moreover, it is interesting to remark from Figs. 3 and 4(a) that the second-order estimates—though strictly below—are practically indistinguishable from the Voigt bound. In this regard, it is fitting to recall that for the case of *applied axisymmetric shear* of fiber-reinforced elastomers with *incompressible, isotropic* matrix phase and *incompressible, isotropic* fibers, the Voigt bound can be shown to be an *exact* result for the effective stored-energy function \hat{W} , regardless of the shape, orientation, and distribution of the fibers in the transverse plane (e.g., here, the \mathbf{e}_1 – \mathbf{e}_2 plane). In view of the relatively high values of the bulk moduli of the matrix phase, $\kappa^{(1)}/\mu^{(1)} = 50$, and the fibers, $\kappa^{(2)}/\mu^{(1)} = 1000$, this suggests that the Voigt bound—and hence

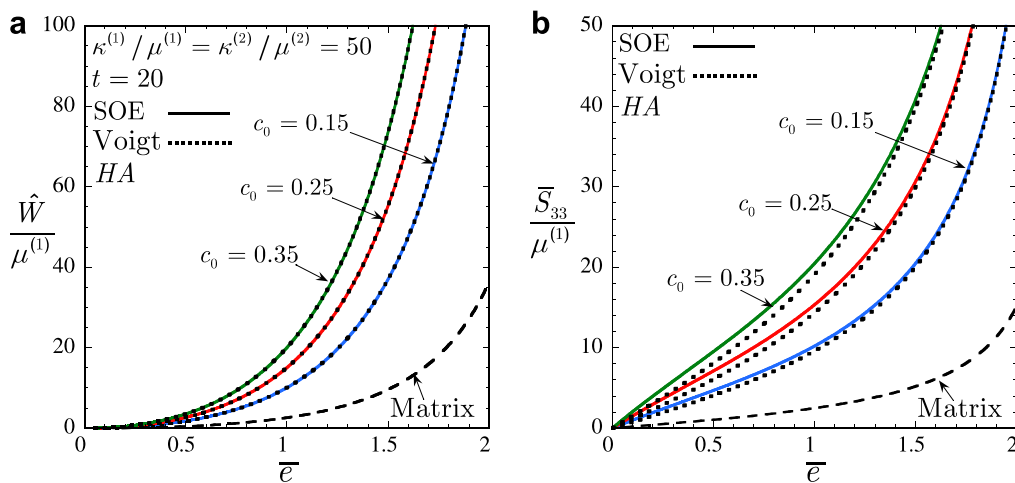


Fig. 3. Effective response, as predicted by the second-order estimate (SOE) and the Voigt bound, of a fiber-reinforced elastomer subjected to “tensile” axisymmetric shear: $\bar{\mathbf{F}} = \bar{\lambda}_1 \mathbf{e}_1 \otimes \mathbf{e}_1 + \bar{\lambda}_2 \mathbf{e}_2 \otimes \mathbf{e}_2 + \bar{\lambda}_3 \mathbf{e}_3 \otimes \mathbf{e}_3$ with $\bar{\lambda}_3 = \bar{\lambda} \geq 1$ and $\bar{\lambda}_1 = \bar{\lambda}_2 = \bar{\lambda}^{-1/2}$. The results correspond to Gent phases with compressibility ratios $\kappa^{(1)}/\mu^{(1)} = \kappa^{(2)}/\mu^{(2)} = 50$, contrast $t = \mu^{(2)}/\mu^{(1)} = 20$, and various values of initial volume fraction of fibers c_0 , and are shown as a function of the logarithmic strain $\bar{e} = \ln \bar{\lambda}$. (a) The normalized effective stored-energy function $\hat{W}/\mu^{(1)}$. (b) The normalized stress component $\bar{S}_{33}/\mu^{(1)} = (1/\mu^{(1)})\partial\hat{W}/\partial\bar{F}_{33}$.

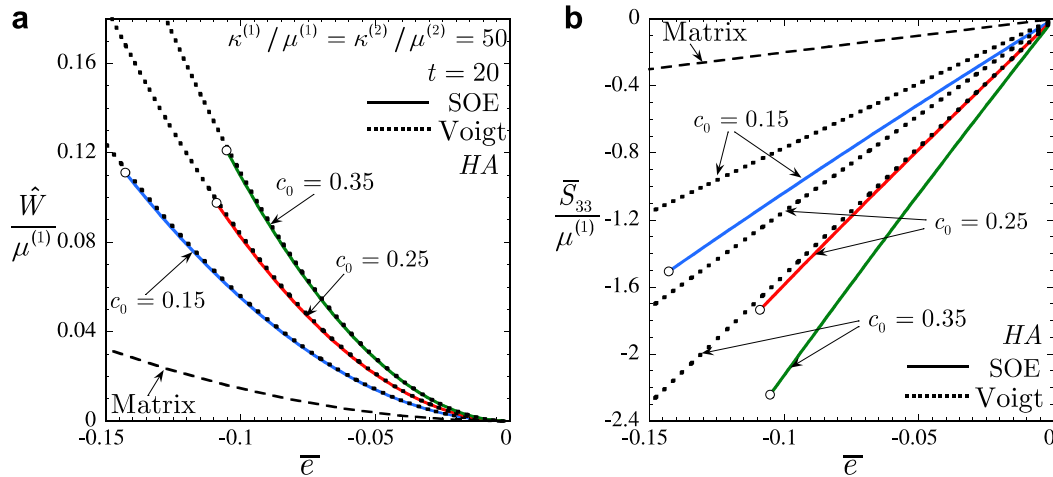


Fig. 4. Effective response of a fiber-reinforced elastomer subjected to “compressive” axisymmetric shear: $\bar{\mathbf{F}} = \bar{\lambda}_1 \mathbf{e}_1 \otimes \mathbf{e}_1 + \bar{\lambda}_2 \mathbf{e}_2 \otimes \mathbf{e}_2 + \bar{\lambda}_3 \mathbf{e}_3 \otimes \mathbf{e}_3$ with $\bar{\lambda}_3 = \bar{\lambda} \leq 1$ and $\bar{\lambda}_1 = \bar{\lambda}_2 = \bar{\lambda}^{-1/2}$. The results correspond to Gent phases with compressibility ratios $\kappa^{(1)}/\mu^{(1)} = \kappa^{(2)}/\mu^{(2)} = 50$, contrast $t = \mu^{(2)}/\mu^{(1)} = 20$, and various values of initial volume fraction of fibers c_0 , and are shown as a function of the logarithmic strain $\bar{e} = \ln \bar{\lambda}$. (a) The normalized effective stored-energy function $\hat{W}/\mu^{(1)}$. (b) The normalized stress component $\bar{S}_{33}/\mu^{(1)} = (1/\mu^{(1)})\partial\hat{W}/\partial\bar{F}_{33}$.

the second-order estimates—shown in Figs. 3 and 4(a) are actually very good approximations to the corresponding exact results. Parenthetically, it is also appropriate to record here that, under axisymmetric shear (and only in this case), the second-order estimate (40) can be shown to reduce to the Voigt bound (27) in the limit of overall incompressibility of the material (i.e., $\kappa^{(1)} \rightarrow \infty$ and $\kappa^{(2)} \rightarrow \infty$), thus recovering the exact result. Next, it is recognized from Figs. 3 and 4 that—according to the SOE results—the overall response of the fiber-reinforced elastomer under axisymmetric tension is radically different from its response under axisymmetric compression. Indeed, under axisymmetric tension, the material stiffens until it eventually locks up at an approximate strain of $\bar{e} = 2.3$ (irrespective of the initial volume fraction of fibers c_0). On the other hand, under axisymmetric compression, the material stiffens monotonically, but it also becomes unstable—through loss of strong ellipticity—at relatively small values of strain. More specifically, all the results shown in Fig. 4 lose strong ellipticity because of the vanishing of the effective incremental shear moduli $\hat{\mathcal{L}}_{1313}$ and $\hat{\mathcal{L}}_{2323}$. This implies that the homogenized material may develop *localized shear deformations* in planar zones with normal—in the deformed configuration— $\mathbf{n} = \mathbf{e}_3$, and in the directions $\mathbf{m} \in \text{Span}\{\mathbf{e}_1, \mathbf{e}_2\}$. This response is rather subtle and merits further explanation. When subjected to axisymmetric compression, as shown by Fig. 4(b), the fiber-reinforced elastomer *stiffens*—due to the constitutive stiffening of the matrix phase and the fibers—in the “direction” of the applied loading (i.e., $\hat{\mathcal{L}}_{3333}$ increases with the applied stretch). However, its overall incremental shear response (perpendicular to the direction of the fibers) *softens* to the point that the material loses strong ellipticity at some finite stretch (at which $\hat{\mathcal{L}}_{1313} = \hat{\mathcal{L}}_{2323} = 0$). This remarkable behavior predicted by the second-order estimate (and *not* by the Voigt bound, as explained in more detail below) is in agreement with experimental evidence (see, for instance, Kyriakides and Ruff, 1997), where the observed failure mode in fiber-reinforced composites subjected to compressive deformation in the fiber direction leads to kink band type instabilities. The interested reader is referred to Merodio and Pence (2001a,b) and Merodio and Ogden (2003) for continuum-mechanics-based studies of kink bands in fiber-reinforced hyperelastic solids.

We conclude the discussion of Figs. 3 and 4 by making the following two remarks. First, it is important to note that in spite of being a very good estimate for the effective stored-energy function \hat{W} of fiber-reinforced elastomers subjected to axisymmetric shear (provided that the bulk moduli of the matrix phase, $\kappa^{(1)}$, and the fibers, $\kappa^{(2)}$, are sufficiently large), the Voigt bound remains strongly elliptic *for all* applied deformations, in disagreement with physical evidence (and with the second-order predictions). This can be readily checked by realizing that the Voigt bound (27), which is essentially the arithmetic average of the local behavior of the matrix phase and the fibers, is a strictly polyconvex function of the applied deformation gradient $\bar{\mathbf{F}}$ and

hence strongly elliptic, as already pointed out in Section 4.2. Second, the corresponding stress–strain results for a *periodic square* distribution of fibers are essentially identical to those illustrated in Figs. 3 and 4 for the periodic hexagonal distribution. This is to be expected since the Voigt bound for \hat{W} , which agrees with the second-order estimates in the context of Figs. 3 and 4, is a *microstructure-independent* result (i.e., it only depends on the volume fraction of the phases).

Fig. 5 provides plots associated with the results shown in Fig. 4 for the critical strain, $\bar{e}_{crit} = \ln \bar{\lambda}_{crit}$, at which the homogenized response of the fiber-reinforced elastomer loses strong ellipticity for: (a) contrasts $t = \mu^{(2)}/\mu^{(1)} = 2$ and 5, and compressibility ratios $\kappa^{(1)}/\mu^{(1)} = \kappa^{(2)}/\mu^{(2)} = 50$, as a function of the initial volume fraction of fibers c_0 ; and (b) compressibility ratios $\kappa^{(1)}/\mu^{(1)} = \kappa^{(2)}/\mu^{(1)} = 1, 5$, and 50, and fiber volume fraction $c_0 = 25\%$, as a function of the contrast t . A key observation that should be made from Fig. 5 is that, under axisymmetric shear compression, the fiber-reinforced elastomer becomes unstable at smaller compressive strains \bar{e}_{crit} for higher values of the contrast t . In fact, it can be shown that $\bar{e}_{crit} \rightarrow 0$ as $t \rightarrow \infty$. That is, for the case when the fibers are taken to be rigid (i.e., for $t = \infty$), the fiber-reinforced elastomer is already unstable at zero strain when subjected to axisymmetric shear compression. Of course, an elastomer reinforced with rigid fibers is itself rigid under loading conditions that require deformation of the fibers. The issue here is that in spite of being rigid (in the principal solution), the material is actually unstable when subjected to axisymmetric shear compression along the fiber direction.

Fig. 5(a) shows that $\bar{e}_{crit} \rightarrow -\infty$ as $c_0 \rightarrow 0$. This is consistent with the fact that the elastomeric matrix phase of the material is strongly elliptic, so that in the absence of fibers (i.e., for $c_0 = 0$) the material remains stable for all deformations. As the initial volume fraction of fibers c_0 is increased from zero, the critical strain at which the material loses strong ellipticity \bar{e}_{crit} increases monotonically up to a certain $c_0 < 50\%$ at which \bar{e}_{crit} reaches a maximum. After this point, further increase in c_0 results in a monotonic decrease of \bar{e}_{crit} . This behavior can be easily explained by recognizing that the fibers are strongly elliptic, so that in the limit as $c_0 \rightarrow 1$, \bar{e}_{crit} is expected to become unbounded. Note, however, that the limiting value $c_0 = 1$ cannot be actually reached, since for the periodic hexagonal distribution of fibers under consideration here, fiber contact takes place (in the undeformed configuration) at $c_0 = \pi/(2\sqrt{3}) \approx 91\%$, as indicated in Fig. 5(a) by the symbol “•.” Finally, it is interesting to note that the inverted “U-shape” of the loss of strong ellipticity curves shown in Fig. 5(a) is reminiscent of the corresponding *exact* result for two-phase laminates (Triantafyllidis and Maker, 1985), which have been considered by various authors as 2D models for fiber-reinforced materials (see, e.g., Triantafyllidis and Maker, 1985, and Kyriakides et al., 1995).

Fig. 5(b) shows that the homogenized response of the fiber-reinforced elastomer loses strong ellipticity at smaller critical strains \bar{e}_{crit} for higher values of the bulk moduli of the elastomeric matrix phase, $\kappa^{(1)}$, and of the

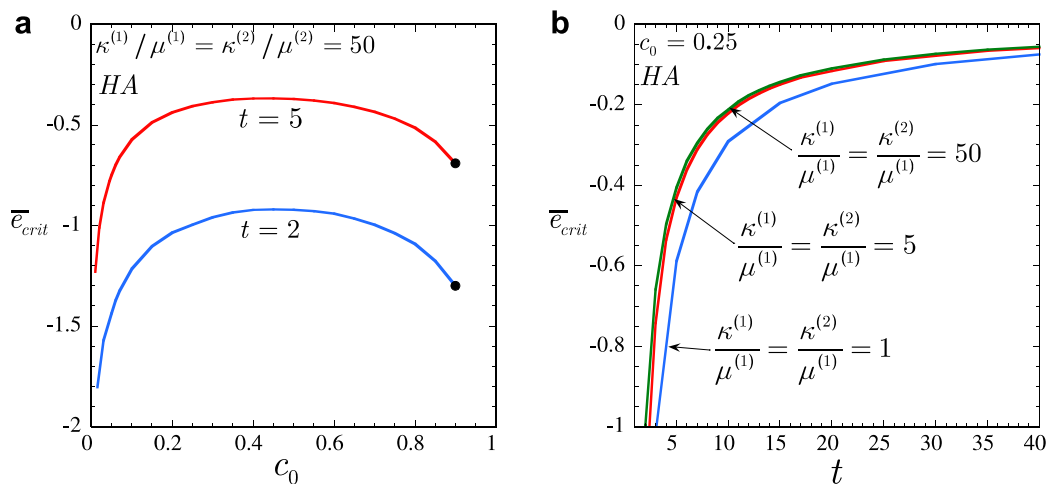


Fig. 5. Axisymmetric shear ($\bar{\mathbf{F}} = \bar{\lambda}^{-1/2}\mathbf{e}_1 \otimes \mathbf{e}_1 + \bar{\lambda}^{-1/2}\mathbf{e}_2 \otimes \mathbf{e}_2 + \bar{\lambda}\mathbf{e}_3 \otimes \mathbf{e}_3$) of a Gent elastomer reinforced with aligned, cylindrical Gent fibers distributed periodically in a hexagonal arrangement (HA). (a) The critical strain $\bar{e}_{crit} = \ln \bar{\lambda}_{crit}$ at which the homogenized fiber-reinforced elastomer loses strong ellipticity for two values of the contrast $t = \mu^{(2)}/\mu^{(1)}$, as a function of the initial volume fraction of fibers c_0 . (b) The critical strain \bar{e}_{crit} for various values of the compressibility ratios $\kappa^{(1)}/\mu^{(1)} = \kappa^{(2)}/\mu^{(1)}$, as a function of the contrast t .

fibers, $\kappa^{(2)}$. That is, in strain space, the less compressible the more unstable the material is. Interestingly, this trend has also been observed in other material systems (see, e.g., Triantafyllidis et al., 2006; Lopez-Pamies and Ponte Castañeda, 2006b; Michel et al., in press).

Finally, it is fitting to mention that the corresponding results for a periodic square distribution of fibers are essentially identical to those illustrated in Fig. 5 for the periodic hexagonal distribution, with the exception that the onset of fiber contact in Fig. 5(a) would then take place at $c_0 = \pi/4 \approx 79\%$, as opposed to $c_0 = \pi/(2\sqrt{3}) \approx 91\%$. This result, together with the observations made from Figs. 3 and 4, suggest that not only the overall stress–strain relation, but also the macroscopic stability of fiber-reinforced elastomers subjected to axisymmetric shear are controlled mainly by the contrast between the elastomeric matrix phase and the fibers and their respective volume fractions, and not so much by the in-plane fiber distribution.

5.2. In-plane pure shear

Fig. 6 provides plots for the effective behavior of Gent elastomers reinforced with periodic square (SA) and hexagonal (HA) distributions of Gent fibers for in-plane pure shear loading. More specifically, for both distributions, results are presented for pure shear loading aligned with the principal axes of the microstructure $\{\mathbf{e}_i\}$ (later referred to as pure shear in the $[1, 0, 0]$ direction): $\bar{\mathbf{F}} = \bar{\lambda}_1 \mathbf{e}_1 \otimes \mathbf{e}_1 + \bar{\lambda}_2 \mathbf{e}_2 \otimes \mathbf{e}_2 + \bar{\lambda}_3 \mathbf{e}_3 \otimes \mathbf{e}_3$ with $\bar{\lambda}_1 = \bar{\lambda}$, $\bar{\lambda}_2 = \bar{\lambda}^{-1}$, and $\bar{\lambda}_3 = 1$ (see Fig. 2). For the SA distribution, results are also presented for pure shear loading oriented at 45° with respect to $\{\mathbf{e}_i\}$ (later referred to as pure shear in the $[1, 1, 0]$ direction): $\bar{\mathbf{F}} = (\bar{\lambda} + \bar{\lambda}^{-1})/2(\mathbf{e}_1 \otimes \mathbf{e}_1 + \mathbf{e}_2 \otimes \mathbf{e}_2) + (\bar{\lambda} - \bar{\lambda}^{-1})/2(\mathbf{e}_1 \otimes \mathbf{e}_2 + \mathbf{e}_2 \otimes \mathbf{e}_1) + \mathbf{e}_3 \otimes \mathbf{e}_3$ (see Fig. 2). (Note that this last loading is denoted by SA₄₅ in the plots.) Results are given for compressibility ratios $\kappa^{(1)}/\mu^{(1)} = 50$ and $\kappa^{(2)}/\mu^{(2)} = 30$, contrast $t = \mu^{(2)}/\mu^{(1)} = 50$, and fiber volume fraction $c_0 = 25\%$, as function of the logarithmic strain $\bar{e} = \ln \bar{\lambda}$. Part (a) shows the normalized stored-energy function $\hat{W}/\mu^{(1)}$ and part (b), the normalized non-zero stress components $\bar{S}_{11}/\mu^{(1)}$, $\bar{S}_{22}/\mu^{(1)}$, $\bar{S}_{33}/\mu^{(1)}$ written with respect to the macroscopic Lagrangian principal axes—denoted here by $\{\mathbf{u}_i\}$. In this connection, note that for pure shear loading in the $[1, 0, 0]$ direction: $\mathbf{u}_i = \mathbf{e}_i$ ($i = 1, 2, 3$); while for pure shear loading in the $[1, 1, 0]$ direction: $\mathbf{u}_1 = \sqrt{2}/2(\mathbf{e}_1 + \mathbf{e}_2)$, $\mathbf{u}_2 = \sqrt{2}/2(\mathbf{e}_2 - \mathbf{e}_1)$, $\mathbf{u}_3 = \mathbf{e}_3$.

First, we remark from Fig. 6(a) that the second-order estimates are well below the rigorous Voigt upper bound. This result is consistent with the fact that, under the in-plane loading conditions considered in Fig. 6, the Voigt bound—unlike the second-order estimates and in contradiction with physical evidence—

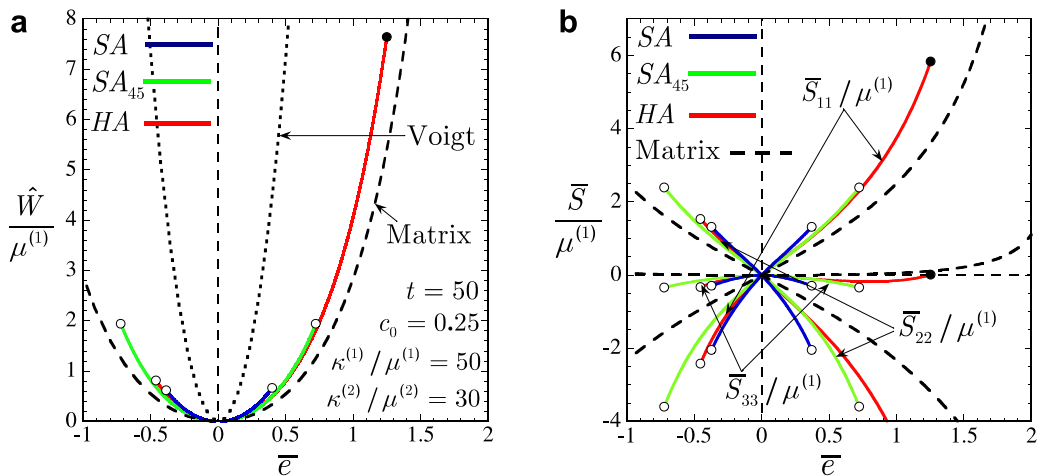


Fig. 6. In-plane pure shear (aligned $\bar{\mathbf{F}} = \bar{\lambda} \mathbf{e}_1 \otimes \mathbf{e}_1 + \bar{\lambda}^{-1} \mathbf{e}_2 \otimes \mathbf{e}_2 + \mathbf{e}_3 \otimes \mathbf{e}_3$ and at a 45° angle $\bar{\mathbf{F}} = (\bar{\lambda} + \bar{\lambda}^{-1})/2(\mathbf{e}_1 \otimes \mathbf{e}_1 + \mathbf{e}_2 \otimes \mathbf{e}_2) + (\bar{\lambda} - \bar{\lambda}^{-1})/2(\mathbf{e}_1 \otimes \mathbf{e}_2 + \mathbf{e}_2 \otimes \mathbf{e}_1) + \mathbf{e}_3 \otimes \mathbf{e}_3$) of a fiber-reinforced elastomer. The results, which are given for periodic square (SA and SA₄₅) and hexagonal (HA) arrangement of fibers, correspond to Gent phases with compressibility ratios $\kappa^{(1)}/\mu^{(1)} = 50$ and $\kappa^{(2)}/\mu^{(2)} = 30$, contrast $t = \mu^{(2)}/\mu^{(1)} = 50$, and fiber volume fraction $c_0 = 25\%$, and are shown as a function of the logarithmic strain $\bar{e} = \ln \bar{\lambda}$. (a) The normalized effective stored-energy function $\hat{W}/\mu^{(1)}$. (b) The normalized stress components $\bar{S}_{11}/\mu^{(1)}$, $\bar{S}_{22}/\mu^{(1)}$, $\bar{S}_{33}/\mu^{(1)}$ written with respect to the macroscopic Lagrangian principal axes.

becomes infinite as the fibers tend to become rigid. The fibers considered in Fig. 6 are not exactly rigid, but the relatively high contrast of $t = 50$ between the matrix phase and the fibers already reveals the asymptotic character of the Voigt bound as $t \rightarrow \infty$. Fig. 6(a) also shows that the effective behavior of the fiber-reinforced material is stiffer than that of the matrix phase, as expected on physical grounds. Another important observation from Fig. 6(a) is the overall anisotropic response of the composite, which is entirely due to the anisotropic initial arrangement of the fibers. More precisely, the overall behavior of the reinforced elastomer with the square arrangement of fibers (see Fig. 2(a)) is seen to be different for pure shear loading in the $[1, 0, 0]$ direction (SA) than in the direction $[1, 1, 0]$ (SA_{45}). In particular, the $[1, 0, 0]$ results appear to be stiffer. This interesting behavior will be explained below, within the context of Fig. 6(b). Furthermore, as a consequence of the overall, in-plane, square symmetry of the material, we also note that the results for tension (i.e., for $\bar{\epsilon} \geq 0$) are indistinguishable from those for compression (i.e., for $\bar{\epsilon} \leq 0$). In contrast, for the hexagonal arrangement (HA) of fibers (see Fig. 2(b)), the effective behavior of the reinforced elastomer is different for tension ($\bar{\epsilon} \geq 0$) than for compression ($\bar{\epsilon} \leq 0$).

Before proceeding with the discussion of the stress–strain results illustrated in Fig. 6(b), it proves helpful to make the following remark. Under the present in-plane loading conditions, the two major underlying mechanisms governing the overall response of the fiber-reinforced elastomers are: the *constitutive stiffening/softening* of the matrix phase with increasing strain, and the *geometric stiffening/softening* effects due to the evolution of the *distribution* of the fibers. The constitutive and geometric effects due to the straining and the evolution of the volume fraction, shape, and orientation of the fibers are negligible. This is because the fibers—which are 50 times stiffer than the matrix phase—remain essentially undeformed along the entire deformation process.

For tensile loadings ($\bar{\epsilon} \geq 0$), Fig. 6(b) illustrates that for all three cases, SA , SA_{45} , and HA , the in-plane stress component $\bar{S}_{11}/\mu^{(1)}$ increases monotonically with increasing strain. The other in-plane stress component, $\bar{S}_{22}/\mu^{(1)}$, is seen to decrease monotonically with increasing $\bar{\epsilon}$, but at a much more rapid rate than $\bar{S}_{11}/\mu^{(1)}$. This disparity is consistent with the fact that, in the direction of the Lagrangian principal axis \mathbf{u}_1 —in which tension is applied—the fibers get farther apart as the deformation progresses, whereas in the direction of the Lagrangian principal axis \mathbf{u}_2 —in which compression is applied—they get closer. The former mechanism induces *geometric* softening on the material and the latter, stiffening. Note that this mechanism is also consistent with the fact that the SA results are stiffer than the SA_{45} ones, since at any given value of the applied strain $\bar{\epsilon}$, the fibers are closer to one another in the $[1, 0, 0]$ direction than in the direction $[1, 1, 0]$. In addition, it is interesting to note from Fig. 6(b) that a considerably large—but smaller than $\bar{S}_{22}/\mu^{(1)}$ —compressive stress $\bar{S}_{33}/\mu^{(1)}$ develops in the fiber direction as the strain increases. Note that analogous comments apply to the results for compressive loading ($\bar{\epsilon} \leq 0$).

Finally, we remark from Fig. 6 that the material with the square arrangement of fibers becomes unstable—through loss of strong ellipticity—under both types of pure shear conditions (SA and SA_{45}), with the SA results losing strong ellipticity at smaller strains. On the other hand, the material with the hexagonal distribution of fibers is seen to lose strong ellipticity only under compression ($\bar{\epsilon} \leq 0$), whereas fiber contact is detected under tension ($\bar{\epsilon} \geq 0$) before any macroscopic instability takes place. Interestingly, for all the above-mentioned cases in which macroscopic instabilities do develop, strong ellipticity is consistently lost due to the vanishing of the incremental shear response perpendicular to the direction of maximum applied compressive strain. For instance, for the SA and HA cases with $\bar{\epsilon} \leq 0$, strong ellipticity is lost due to the vanishing of $\hat{\mathcal{L}}_{2121}$, while for the SA case with $\bar{\epsilon} \geq 0$, strong ellipticity is lost due to the vanishing of $\hat{\mathcal{L}}_{1212}$. This means that, under in-plane pure shear loading, the homogenized fiber-reinforced elastomer may develop *localized shear* deformations in planar zones with normal in the deformed configuration \mathbf{n} , given by the macroscopic Lagrangian principal axis associated with the smallest principal stretch (i.e., the maximum compressive strain), and in the in-plane direction perpendicular to such axis (i.e., the unit vector \mathbf{m} for which condition (10) ceases to hold true is such that $\mathbf{m} \cdot \mathbf{n} = \mathbf{m} \cdot \mathbf{e}_3 = 0$). Making contact now with the microstructure, it is interesting to note that the normal \mathbf{n} corresponds actually to the in-plane direction in which neighboring fibers are closest. This behavior, which is somewhat similar to the one observed for axisymmetric compression, is rather subtle. Indeed, when subjected to in-plane pure shear loading, the overall response of the fiber-reinforced elastomer *stiffens*—as a consequence, partly, of the reinforcing fibers coming closer—in the direction of the maximum applied compressive strain, \mathbf{n} . However, its overall incremental shear response perpendicular to \mathbf{n} *softens* to the point that the material may become macroscopically unstable at some finite stretch. To conclude the

discussion of Fig. 6, it should be mentioned that this remarkable behavior predicted by the second-order estimate (40) is in agreement with the recent numerical (F.E.M.) results of Triantafyllidis et al. (2006) for the in-plane behavior of fiber-reinforced elastomers.

Figs. 7 and 8 illustrate the influence of the initial volume fraction of fibers, c_0 , and the shear contrast, $t = \mu^{(2)}/\mu^{(1)}$, on the effective stress–strain relation of fiber-reinforced elastomers with Gent (matrix and fiber phases) subjected to pure shear loading conditions. For conciseness, results are provided for *aligned* pure shear loading ($\bar{\mathbf{F}} = \bar{\lambda}\mathbf{e}_1 \otimes \mathbf{e}_1 + \bar{\lambda}^{-1}\mathbf{e}_2 \otimes \mathbf{e}_2 + \mathbf{e}_3 \otimes \mathbf{e}_3$) and an initially hexagonal distribution (HA) of fibers. However, it should be emphasized that the results presented in Figs. 7 and 8 are similar to those obtained for “misaligned” pure shear loadings, as well as for different initial fiber distributions.

Fig. 7 displays results for the normalized effective stress components $\bar{S}_{11}/\mu^{(1)}$, $\bar{S}_{22}/\mu^{(1)}$, $\bar{S}_{33}/\mu^{(1)}$ for fiber-reinforced Gent elastomers with compressibility ratios $\kappa^{(1)}/\mu^{(1)} = 50$, $\kappa^{(2)}/\mu^{(2)} = 30$, contrast $t = \mu^{(2)}/\mu^{(1)} = 50$, and

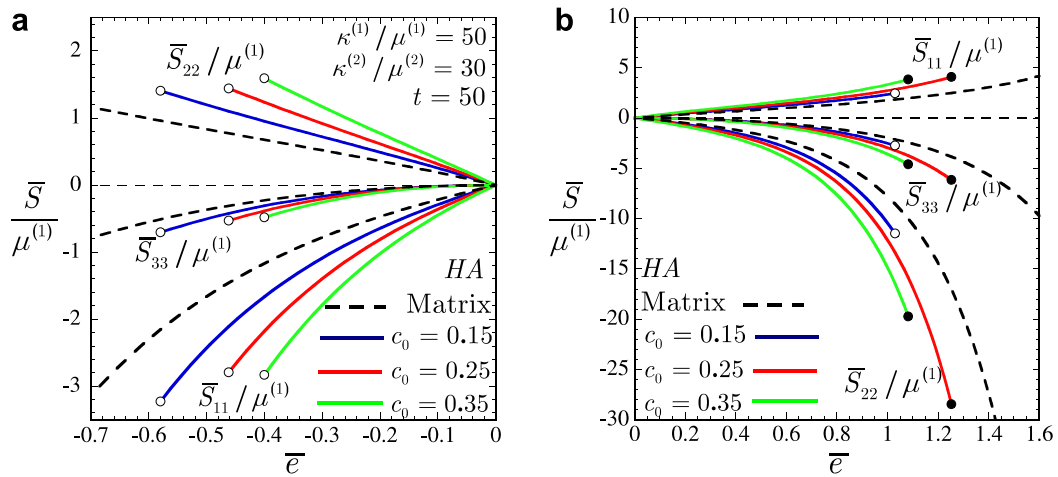


Fig. 7. In-plane aligned pure shear ($\bar{\mathbf{F}} = \bar{\lambda}\mathbf{e}_1 \otimes \mathbf{e}_1 + \bar{\lambda}^{-1}\mathbf{e}_2 \otimes \mathbf{e}_2 + \mathbf{e}_3 \otimes \mathbf{e}_3$) of a fiber-reinforced Gent elastomer with an initially hexagonal arrangement (HA) of fibers. The results correspond to compressibility ratios $\kappa^{(1)}/\mu^{(1)} = 50$, $\kappa^{(2)}/\mu^{(2)} = 30$, contrast $t = \mu^{(2)}/\mu^{(1)} = 50$, and initial volume fractions $c_0 = 15, 25$ and 35% . The normalized stress components $\bar{S}_{11}/\mu^{(1)}$, $\bar{S}_{22}/\mu^{(1)}$, $\bar{S}_{33}/\mu^{(1)}$ for: (a) pure shear compression $\bar{e} \leq 0$, and (b) pure shear tension $\bar{e} \geq 0$.

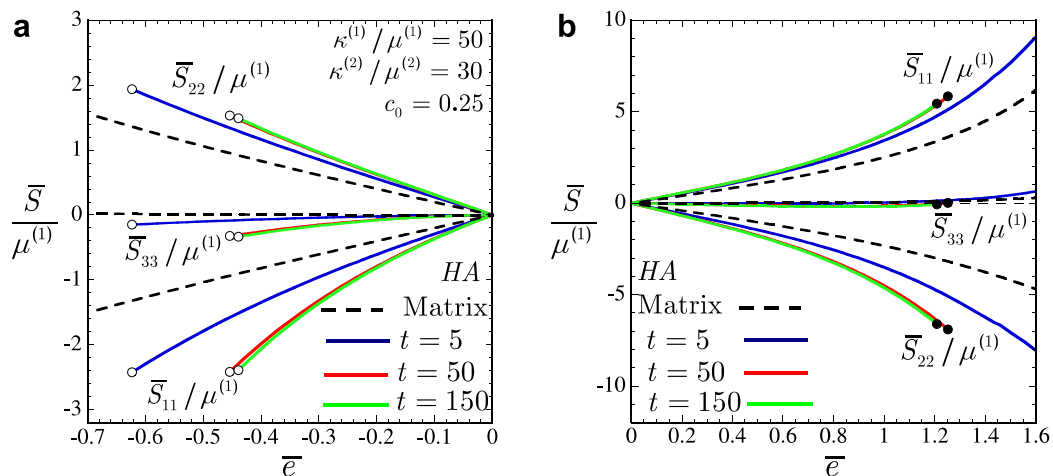


Fig. 8. In-plane aligned pure shear ($\bar{\mathbf{F}} = \bar{\lambda}\mathbf{e}_1 \otimes \mathbf{e}_1 + \bar{\lambda}^{-1}\mathbf{e}_2 \otimes \mathbf{e}_2 + \mathbf{e}_3 \otimes \mathbf{e}_3$) of a fiber-reinforced Gent elastomer with an initially hexagonal arrangement (HA) of fibers. The results correspond to compressibility ratios $\kappa^{(1)}/\mu^{(1)} = 50$, $\kappa^{(2)}/\mu^{(2)} = 30$, initial volume fraction $c_0 = 0.25$ and shear contrasts $t = \mu^{(2)}/\mu^{(1)} = 5, 50$, and 150 . The normalized stress components $\bar{S}_{11}/\mu^{(1)}$, $\bar{S}_{22}/\mu^{(1)}$, $\bar{S}_{33}/\mu^{(1)}$ for: (a) pure shear compression $\bar{e} \leq 0$, and (b) pure shear tension $\bar{e} \geq 0$.

initial volume fractions $c_0 = 15, 25,$ and 35% , as a function of the logarithmic strain $\bar{\epsilon} = \ln \bar{\lambda}$. Part (a) shows results for aligned pure shear compression ($\bar{\epsilon} \leq 0$), and part (b), for aligned pure shear tension ($\bar{\epsilon} \geq 0$). The increase of the initial volume fraction of fibers c_0 can be seen to have three major effects on the effective stress–strain relation of the reinforced elastomer. First, the overall behavior of the material is stiffer. Second, in spite of the fact that the material is stiffer, it is also less stable, as loss of strong ellipticity occurs at smaller strains. Finally, fiber contact is also seen to occur at smaller finite strains. All these three effects are consistent with the fact that increasing the volume fraction of the fibers corresponds effectively to increasing the relative size of the *reinforcing* inclusions in the material. Indeed, “bigger” stiffer fibers are expected to lead to an overall stiffer behavior. Further, “bigger” fibers imply that neighboring fibers are closer to one another. Thus, according to preceding discussions, closer fibers lead to *softer* effective incremental shear moduli, which, in turn, lead to smaller critical strains at loss of strong ellipticity. Moreover, closer fibers clearly lead to smaller macroscopic strains at fiber contact.

Fig. 8 displays corresponding results for fiber-reinforced Gent elastomers with compressibility ratios $\kappa^{(1)}/\mu^{(1)} = 50, \kappa^{(2)}/\mu^{(2)} = 30$, initial volume fraction $c_0 = 0.25$ and shear contrasts $t = \mu^{(2)}/\mu^{(1)} = 5, 50, 150$, as a function of the logarithmic strain $\bar{\epsilon} = \ln \bar{\lambda}$. Part (a) shows results for aligned pure shear compression ($\bar{\epsilon} \leq 0$), and part (b), for aligned pure shear tension ($\bar{\epsilon} \geq 0$). As expected on physical grounds, increasing the shear contrast t is seen to lead to an overall stiffer behavior of the composite. In addition, and similar to increasing fiber volume fraction, increasing the shear contrast t is seen to lead to smaller critical strains at which loss of strong ellipticity and fiber contact take place. These trends are a direct consequence of the fact that by increasing t , the average deformation in the matrix phase increases—and, by the same token, the average deformation in fibers decreases. As a result, neighboring fibers get closer leading—as explained above—to the onset of instabilities and fiber contact at smaller strains.

Fig. 9 illustrates the influence of the initial distribution of fibers (*SA* vs. *HA*), initial fiber volume fraction, c_0 , and shear contrast, $t = \mu^{(2)}/\mu^{(1)}$, on the onset of macroscopic instabilities in fiber-reinforced Gent elastomers. In particular, *SA* and *HA* results are shown for *aligned* pure shear loading $\bar{\mathbf{F}} = \bar{\lambda} \mathbf{e}_1 \otimes \mathbf{e}_1 + \bar{\lambda}^{-1} \mathbf{e}_2 \otimes \mathbf{e}_2 + \mathbf{e}_3 \otimes \mathbf{e}_3$, compressibility ratios $\kappa^{(1)}/\mu^{(1)} = 5, \kappa^{(2)}/\mu^{(2)} = 3$ and $\kappa^{(1)}/\mu^{(1)} = 50, \kappa^{(2)}/\mu^{(2)} = 30$, for: (a) the critical strain, $\bar{\epsilon}_{crit} = \ln \bar{\lambda}_{crit}$, at which the composite loses strong ellipticity for contrast $t = 50$, as a function of the initial fiber volume fraction c_0 ; and (b) $\bar{\epsilon}_{crit}$ for initial volume fraction $c_0 = 0.25$, as a function of the contrast t . It is clear from Fig. 9 that the initial distribution of fibers plays a major role in the development of macroscopic instabilities. More precisely, it is observed that the material with initially square distribution (*SA*) of fibers is more unstable (in strain space) than that one with hexagonal distribution

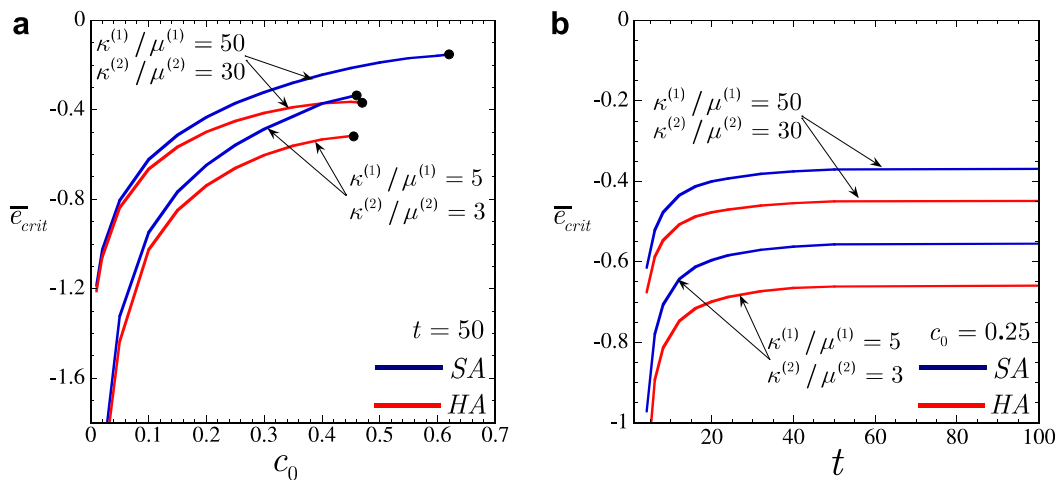


Fig. 9. In-plane aligned pure shear ($\bar{\mathbf{F}} = \bar{\lambda} \mathbf{e}_1 \otimes \mathbf{e}_1 + \bar{\lambda}^{-1} \mathbf{e}_2 \otimes \mathbf{e}_2 + \mathbf{e}_3 \otimes \mathbf{e}_3$) of fiber-reinforced Gent elastomers with initially square (*SA*) and hexagonal (*HA*) arrangements of fibers. (a) The critical strain $\bar{\epsilon}_{crit} = \ln \bar{\lambda}_{crit}$ at which the homogenized fiber-reinforced elastomer loses strong ellipticity, as a function of the initial volume fraction of fibers c_0 . (b) The critical strain $\bar{\epsilon}_{crit}$ as a function of the shear contrast $t = \mu^{(2)}/\mu^{(1)}$. The results are given for various values of compressibility ratios $\kappa^{(1)}/\mu^{(1)}$ and $\kappa^{(2)}/\mu^{(2)}$.

(*HA*). Interestingly, this trend has also been observed in porous elastomers (Michel et al., in press). Furthermore, similar to the axisymmetric shear results shown in Fig. 5(b), Fig. 9 illustrates that for in-plane pure shear, fiber-reinforced elastomers with higher bulk moduli, $\kappa^{(1)}$ and $\kappa^{(2)}$, are more unstable.

Fig. 9(a) shows that the critical strain $\bar{\epsilon}_{\text{crit}}$ is a monotonically increasing function of the initial fiber volume fraction c_0 . In the dilute limit (i.e., $c_0 \rightarrow 0$), $\bar{\epsilon}_{\text{crit}} \rightarrow -\infty$, since the elastomeric matrix is strongly elliptic. Moreover, in this limit, it is interesting to observe that the results for the square (*SA*) and hexagonal (*HA*) distributions of fibers become practically indistinguishable. This implies that as $c_0 \rightarrow 0$, the fibers do not interact with each other, and hence their initial distribution becomes irrelevant. Note further from Fig. 9(a) that for sufficiently large values of c_0 , fiber contact (denoted with the symbol “•” in the plots) precedes loss of strong ellipticity.

Fig. 9(b) shows that $\bar{\epsilon}_{\text{crit}}$ increases monotonically as a function of the contrast $t = \mu^{(2)}/\mu^{(1)}$. In the limit of small contrast (i.e., $t \rightarrow 1$), $\bar{\epsilon}_{\text{crit}} \rightarrow -\infty$, so that the material remains strongly elliptic for all deformations. On the other hand, in the limit as the fibers are taken to be rigid (i.e., $t \rightarrow \infty$), the critical strain at which the material loses strong ellipticity tends to a finite, non-zero asymptotic value $\bar{\epsilon}_{\text{crit}}^\infty$. This is unlike the behavior illustrated in Fig. 5(b) for axisymmetric shear, where $\bar{\epsilon}_{\text{crit}} \rightarrow 0$ in the limit as $t \rightarrow \infty$. The key difference between these two loading conditions is as follows. For axisymmetric shear and large t , the effective stored-energy function (40) can be shown to be of the form $\hat{W} = \hat{W}_t t + O(t^0)$. On the other hand, for in-plane pure shear and large t , $\hat{W} = \hat{W}_0 + O(t^{-1})$. In other words, for axisymmetric shear, the overall behavior of the material becomes rigid when the fibers are taken to be rigid, and as a result, $\bar{\epsilon}_{\text{crit}} \rightarrow 0$ in the limit as $t \rightarrow \infty$. On the contrary, for in-plane pure shear, the effective stored-energy function \hat{W} does not become unbounded when the fibers are taken to be rigid, but instead, it tends to some finite limiting behavior \hat{W}_0 , so that $\bar{\epsilon}_{\text{crit}}^\infty$ need not be zero.

In short, the results illustrated in Figs. 6–9 reveal that the overall behavior of fiber-reinforced elastomers subjected to in-plane pure shear deformations depends very critically on the initial *distribution* and *volume fraction* of the fibers. The dependence on the *contrast* between the elastomeric matrix and fibers, as measured by t , is very significant from small to moderate values of t . For relatively large contrasts (e.g., here, $t > 50$), the behavior of the composite tends to that of elastomers with rigid fibers, and hence, it becomes virtually insensitive to further changes in t . This is unlike the behavior observed for axisymmetric shear deformations (Figs. 3–5), where the dependence on t was critical in the entire physical range $1 \leq t \leq \infty$, and the dependence on the fiber distribution was practically negligible.

5.3. In-plane simple shear

Fig. 10 displays results, as predicted by the second-order estimate (40), for the effective behavior of fiber-reinforced Gent elastomers subjected to in-plane simple shear: $\bar{\mathbf{F}} = \mathbf{I} + \bar{\gamma} \mathbf{e}_1 \otimes \mathbf{e}_2$ with \mathbf{I} denoting the identity operator for second-order tensors, and $\bar{\gamma}$, the amount of shear. In particular, results are shown for initially square (*SA*) and hexagonal (*HA*) distributions of fibers and compressibility ratios $\kappa^{(1)}/\mu^{(1)} = 50$ and $\kappa^{(2)}/\mu^{(2)} = 30$. Part (a) shows the normalized shear stress $\bar{S}_{12}/\mu^{(1)} = (1/\mu^{(1)})\partial\hat{W}/\partial\bar{\gamma}$ for initial volume fractions of fibers $c_0 = 15, 25, 30\%$ and fixed contrast $t = \mu^{(2)}/\mu^{(1)} = 50$, as a function of the amount of shear $\bar{\gamma}$. Part (b) shows the normalized shear stress $\bar{S}_{12}/\mu^{(1)}$ for contrasts $t = 20, 50, 150$ and fixed initial volume fraction $c_0 = 25\%$, as a function of $\bar{\gamma}$. In accord with the results considered in the preceding subsections, Fig. 10(a) shows that the effective behavior of the fiber-reinforced elastomer is stiffer for higher values of c_0 . Similarly, Fig. 10(b) shows that the behavior of the composite is stiffer for higher values of the contrast t . Note, however, that the effect of increasing t is rather weak. Again, this is because the asymptotic behavior of \hat{W} for in-plane deformations and large t is of the form: $\hat{W} = \hat{W}_0 + O(t^{-1})$, as discussed in the previous section. Finally, it is interesting to remark that the effect of the initial distribution of fibers (i.e., *SA* vs. *HA*) on the effective behavior of the composite under in-plane simple shear is negligible at the initial volume fractions of fibers considered. This point is investigated further in the context of the next figure.

Fig. 11 illustrates results for the effective behavior of fiber-reinforced Gent elastomers, with square (*SA*) and hexagonal (*HA*) fiber distributions, subjected to in-plane *pre-compressed* simple shear: $\bar{\mathbf{F}} = \mathbf{I} - 2/5\mathbf{e}_2 \otimes \mathbf{e}_2 + \bar{\gamma}\mathbf{e}_1 \otimes \mathbf{e}_2$. This type of loading condition, which has already been considered by Lahellec et al. (2004) in a somewhat different context, serves to bring out neatly the influence of the initial, as well as

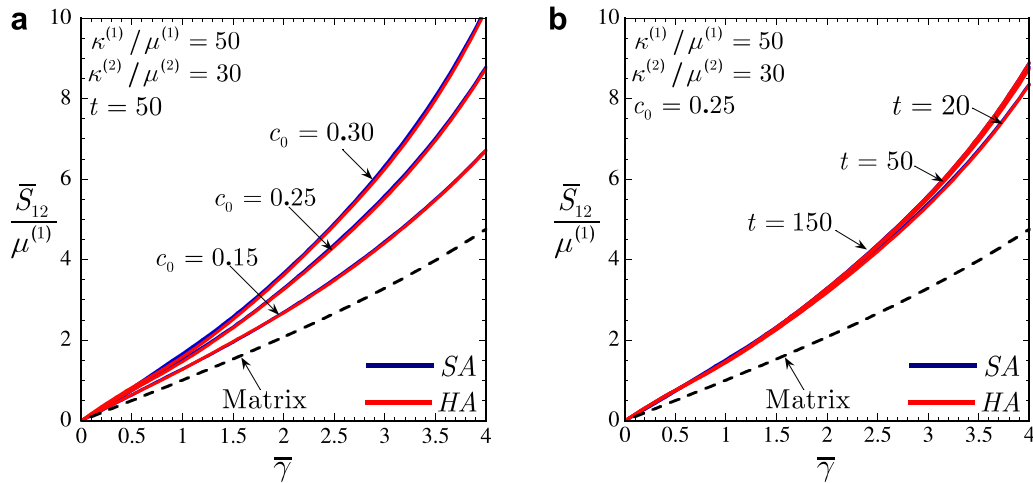


Fig. 10. In-plane simple shear ($\bar{\mathbf{F}} = \mathbf{I} + \bar{\gamma}\mathbf{e}_1 \otimes \mathbf{e}_2$) of a fiber-reinforced elastomer. The results, which are given for periodic square (*SA*) and hexagonal (*HA*) distributions of fibers, correspond to Gent phases with compressibility ratios $\kappa^{(1)}/\mu^{(1)} = 50$ and $\kappa^{(2)}/\mu^{(2)} = 30$. The normalized effective shear stress $\bar{S}_{12}/\mu^{(1)} = (1/\mu^{(1)})\partial\hat{W}/\partial\bar{\gamma}$, as a function of the amount of shear $\bar{\gamma}$ for: (a) contrast $t = \mu^{(2)}/\mu^{(1)} = 50$ and various initial volume fractions c_0 , and (b) for initial volume fraction $c_0 = 25\%$ and various values of the contrast t .

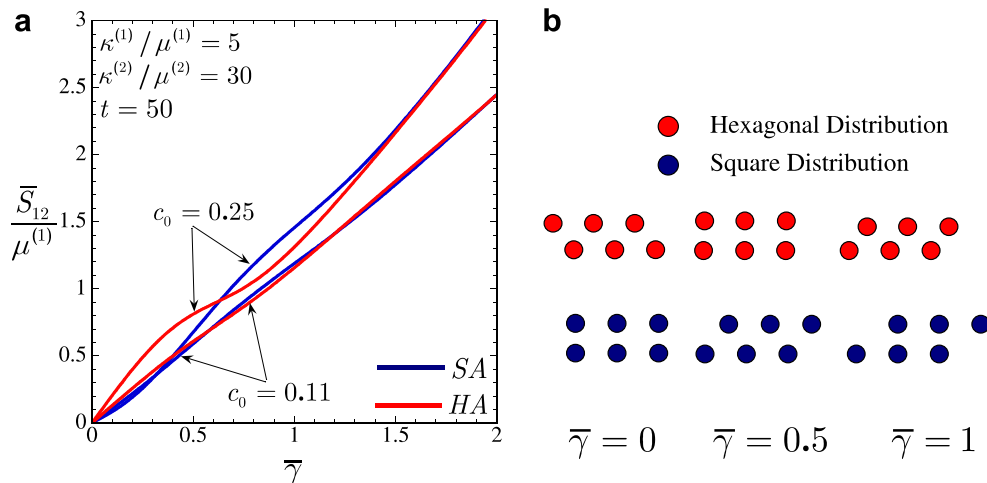


Fig. 11. In-plane pre-compressed simple shear ($\bar{\mathbf{F}} = \mathbf{I} - 2/5\mathbf{e}_2 \otimes \mathbf{e}_2 + \bar{\gamma}\mathbf{e}_1 \otimes \mathbf{e}_2$) of a fiber-reinforced elastomer. The results, which are given for periodic square (*SA*) and hexagonal (*HA*) distributions of fibers, correspond to Gent phases with compressibility ratios $\kappa^{(1)}/\mu^{(1)} = 5$ and $\kappa^{(2)}/\mu^{(2)} = 30$, contrast $t = 50$, and initial volume fraction of fibers $c_0 = 11$ and 25% . (a) The normalized effective shear stress $\bar{S}_{12}/\mu^{(1)} = (1/\mu^{(1)})\partial\hat{W}/\partial\bar{\gamma}$, as a function of the applied amount of shear $\bar{\gamma}$. (b) Schematic representation of the evolution of the distribution of fibers upon loading.

evolving, distribution of fibers on the macroscopic behavior of the composite. Part (a) shows the normalized shear stress $\bar{S}_{12}/\mu^{(1)} = (1/\mu^{(1)})\partial\hat{W}/\partial\bar{\gamma}$ as a function of the amount of shear $\bar{\gamma}$ for compressibility ratios $\kappa^{(1)}/\mu^{(1)} = 5$, $\kappa^{(2)}/\mu^{(2)} = 30$, contrast $t = \mu^{(2)}/\mu^{(1)} = 50$, and initial fiber concentrations $c_0 = 11$ and 25% . Part (b) depicts a schematic representation of the evolution of the fiber distribution along the loading process for both initial arrangement of fibers.

A key observation from Fig. 11(a) is the oscillations exhibited by the macroscopic stress–strain response of the material for both initial (square and hexagonal) distributions of fibers. These oscillations are a direct consequence of the evolution of the microstructure. More specifically, the oscillations are caused by the evolution of the *distribution* of the fibers, which alternates from configurations where the fibers are aligned with other fibers to configurations where the fibers are aligned between two other fibers, as illustrated by Fig. 11(b). Note

that the oscillations are more pronounced for higher values of initial volume fraction, as a consequence of the stronger interactions between the fibers. Note further that for sufficiently large deformations $\bar{\gamma}$, the oscillations die out. In order to understand this behavior, it should be recalled that besides the evolution of the distribution of the fibers, there is another mechanism that governs the overall behavior of the material under in-plane deformations, namely, the constitutive stiffening of the matrix phase due to the straining. For large $\bar{\gamma}$, the matrix *constitutive* stiffening dominates, and the *geometric* effect due to the evolution of the fiber distribution becomes negligible, hence explaining the apparent disappearance of oscillations for large $\bar{\gamma}$ in Fig. 11(a).

No loss of strong ellipticity was detected for any of the results shown in Figs. 10 and 11. However, it should be mentioned that by sufficiently increasing the pre-compressed strain in the \mathbf{e}_2 direction (e.g., from $2/5 = 0.4$ to 0.5) would lead to loss of strong ellipticity at some finite value of the amount of shear $\bar{\gamma}$. Interestingly, the mechanism by which fiber-reinforced elastomers lose strong ellipticity when subjected to in-plane pre-compressed simple shear is entirely analogous to that one detected for in-plane pure shear. Namely, loss of strong ellipticity occurs by the vanishing of the effective incremental shear modulus perpendicular to the direction in which neighboring fibers are closest to each other.

5.4. Out-of-plane pure shear

Figs. 12 and 13 present the effective behavior, as predicted by the second-order estimate (40), of Gent elastomers reinforced with periodic square (SA) and hexagonal (HA) distributions of Gent fibers subjected to out-of-plane pure shear: $\bar{\mathbf{F}} = \bar{\lambda}_1 \mathbf{e}_1 \otimes \mathbf{e}_1 + \bar{\lambda}_2 \mathbf{e}_2 \otimes \mathbf{e}_2 + \bar{\lambda}_3 \mathbf{e}_3 \otimes \mathbf{e}_3$ with $\bar{\lambda}_3 = \bar{\lambda}$, $\bar{\lambda}_1 = \bar{\lambda}^{-1}$, and $\bar{\lambda}_2 = 1$. Fig. 12 illustrates results for tension in the fiber direction (i.e., $\bar{\lambda} \geq 1$) and Fig. 13, for compression (i.e., $\bar{\lambda} \leq 1$). In particular, results are shown for compressibility ratios $\kappa^{(1)}/\mu^{(1)} = \kappa^{(2)}/\mu^{(2)} = 50$ and contrast $t = \mu^{(2)}/\mu^{(1)} = 20$, as a function of the logarithmic strain $\bar{e} = \ln \bar{\lambda}$. Parts (a) show the normalized effective stored-energy function $\hat{W}/\mu^{(1)}$ for initial volume fractions of fibers $c_0 = 15, 25, 35\%$, and parts (b), the normalized stress components $\bar{S}_{11}/\mu^{(1)}$, $\bar{S}_{22}/\mu^{(1)}$, $\bar{S}_{33}/\mu^{(1)}$ for $c_0 = 25\%$.

In accord with the preceding subsections, Figs. 12 and 13 show that the effective behavior of the fiber-reinforced elastomer is stiffer for higher values of c_0 . Consistent with previous results, it is also seen that the second-order estimates satisfy the rigorous Voigt bound. Moreover, it is important to remark that the results displayed in Figs. 12 and 13 indicate that the effective behavior of the fiber-reinforced elastomer—as measured by the effective stored-energy function \hat{W} and macroscopic stress $\bar{\mathbf{S}}$ —for out-of-plane pure shear deformations

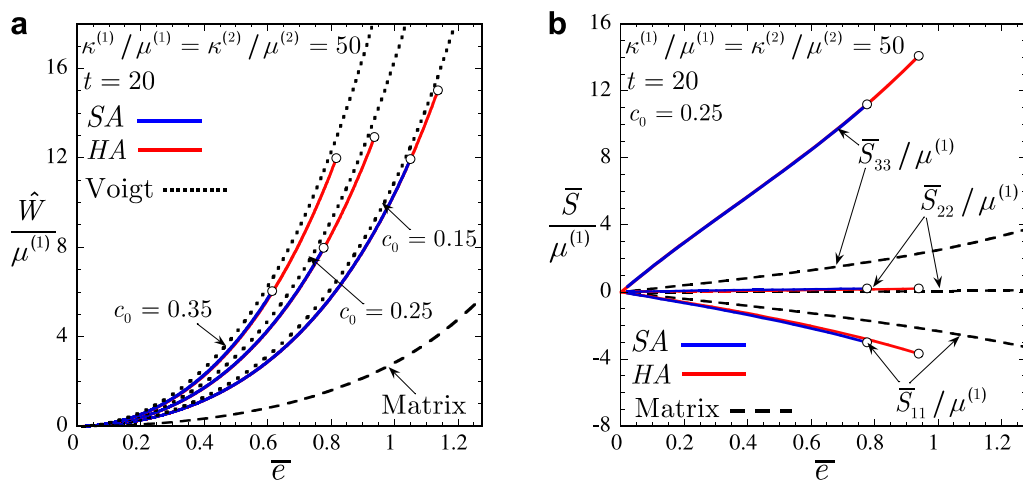


Fig. 12. Effective response of Gent fiber-reinforced elastomers subjected to “tensile” out-of-plane pure shear: $\bar{\mathbf{F}} = \bar{\lambda}_1 \mathbf{e}_1 \otimes \mathbf{e}_1 + \bar{\lambda}_2 \mathbf{e}_2 \otimes \mathbf{e}_2 + \bar{\lambda}_3 \mathbf{e}_3 \otimes \mathbf{e}_3$ with $\bar{\lambda}_3 = \bar{\lambda} \geq 1$, $\bar{\lambda}_1 = \bar{\lambda}^{-1}$, and $\bar{\lambda}_2 = 1$. Results are shown for compressibility ratios $\kappa^{(1)}/\mu^{(1)} = \kappa^{(2)}/\mu^{(2)} = 50$, contrast $t = \mu^{(2)}/\mu^{(1)} = 20$, and various values of initial volume fraction of fibers c_0 , as a function of the logarithmic strain $\bar{e} = \ln \bar{\lambda}$. (a) The normalized effective stored-energy function $\hat{W}/\mu^{(1)}$. (b) The normalized stress components $\bar{S}_{11}/\mu^{(1)}$, $\bar{S}_{22}/\mu^{(1)}$, $\bar{S}_{33}/\mu^{(1)}$.

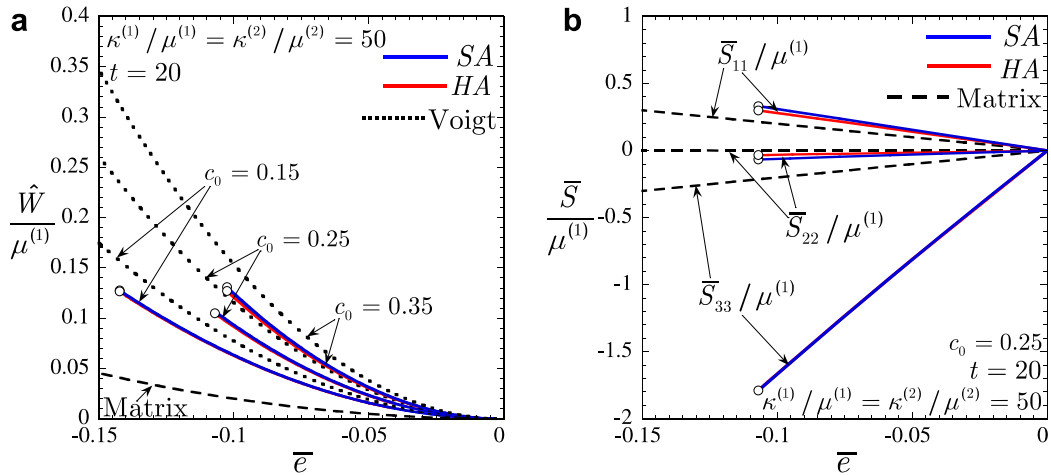


Fig. 13. Effective response of Gent fiber-reinforced elastomers subjected to “compressive” out-of-plane pure shear: $\bar{\mathbf{F}} = \bar{\lambda}_1 \mathbf{e}_1 \otimes \mathbf{e}_1 + \bar{\lambda}_2 \mathbf{e}_2 \otimes \mathbf{e}_2 + \bar{\lambda}_3 \mathbf{e}_3 \otimes \mathbf{e}_3$ with $\bar{\lambda}_3 = \bar{\lambda} \leq 1$, $\bar{\lambda}_1 = \bar{\lambda}^{-1}$, and $\bar{\lambda}_2 = 1$. Results are shown for compressibility ratios $\kappa^{(1)}/\mu^{(1)} = \kappa^{(2)}/\mu^{(2)} = 50$, contrast $t = \mu^{(2)}/\mu^{(1)} = 20$, and various values of initial volume fraction of fibers c_0 , as a function of the logarithmic strain $\bar{e} = \ln \bar{\lambda}$. (a) The normalized effective stored-energy function $\hat{W}/\mu^{(1)}$. (b) The normalized stress components $\bar{S}_{11}/\mu^{(1)}$, $\bar{S}_{22}/\mu^{(1)}$, $\bar{S}_{33}/\mu^{(1)}$.

depends very weakly on the initial distribution of fibers (since the *SA* and *HA* results are very much identical). This behavior is in precise agreement with the results found for axisymmetric shear deformations, which were discussed in the context of Figs. 3 and 4. In this regard, as for axisymmetric shear deformations, the independence on fiber distribution in the present context can be understood by recognizing that out-of-plane pure shear is a *fiber-dominated* mode of deformation. That is, under out-of-plane pure shear, the local strain in the fibers—which are much stiffer than the matrix phase—is comparable to the strain in the elastomeric matrix, and, as a consequence, the effective stored-energy function \hat{W} and macroscopic stress $\bar{\mathbf{S}}$ are controlled primarily by the *contrast* (t) and the fiber *volume fraction* (c_0), and *not* so much by the fiber distribution. Interestingly, this is not true for the effective incremental modulus tensor $\hat{\mathcal{L}}$ —which measures the macroscopic stability of the homogenized material—as discussed next.

Fig. 12 shows that fiber-reinforced elastomers with *SA* and *HA* fiber distributions become unstable—through loss of strong ellipticity—at finite values of deformation when subjected to out-of-plane pure shear with *tension* in the fiber direction. Note, however, that materials with the *SA* distribution lose strong ellipticity at smaller strains than those with the *HA* arrangement of fibers. Interestingly, all the *SA* and *HA* results displayed in Fig. 12 lose strong ellipticity because of the vanishing of the incremental, *in-plane*, shear modulus $\hat{\mathcal{L}}_{2121}$. That is, condition (10) fails for the pair $\mathbf{n} = \mathbf{e}_1$ and $\mathbf{m} = \mathbf{e}_2$. Making contact with the evolution of the microstructure, this failure mechanism—which is exactly the same as the one encountered for *in-plane* pure and simple shear deformations—is caused by the fact that neighboring fibers get closer to each other with the increasing applied deformation. Thus, as for the *in-plane* deformations discussed in the preceding subsection, the onset of macroscopic instabilities for out-of-plane pure shear with tension in the fiber direction depends critically on the overall incremental *in-plane* behavior of the composite, and hence, on the *in-plane* distribution of fibers.

Similar to Fig. 12, 13 shows that fiber-reinforced elastomers with *SA* and *HA* fiber distributions also lose strong ellipticity when subjected to out-of-plane pure shear with *compression* in the fiber direction. In this case, loss of strong ellipticity takes place because of the vanishing of the effective incremental shear modulus $\hat{\mathcal{L}}_{1313}$, which implies that condition (10) fails for the pair $\mathbf{n} = \mathbf{e}_3$ and $\mathbf{m} = \mathbf{e}_1$. This failure mode—similar to the one encountered for axisymmetric shear compression—is consistent with the development of kink band-type instabilities in the fiber-reinforced composite. Note that because of the failure mode is *fiber-dominated* (i.e., $\hat{\mathcal{L}}_{1313} = 0$), the critical strains at which the homogenized material loses strong ellipticity are very much independent of the *in-plane* fiber distribution.

6. Concluding remarks

In this work, we have derived a homogenization-based constitutive model for the overall mechanical behavior of elastomers reinforced with aligned cylindrical fibers subjected to large deformations, by means of the second-order homogenization method (Lopez-Pamies and Ponte Castañeda, 2006a). Although this method applies more generally, in this work, for relative simplicity, it has been applied to materials with generalized Neo-Hookean (matrix and fiber) phases and periodic distribution of fibers. Explicit results have been computed and discussed for fiber-reinforced compressible Gent elastomers with square and hexagonal distribution of fibers subjected to *out-of-plane*, *in-plane* and coupled *in-plane* and *out-of-plane* loading conditions.

By incorporating finer details about the initial microstructural information, such as the fiber shape, orientation, and distribution, the proposed model exhibits orthotropic material symmetry distinguishing between *fiber-* and *matrix-dominated* modes of deformation. Indeed, as illustrated through various representative results, loading conditions that involve deformation in the fiber direction lead to much stiffer model responses than those that do not induce fiber deformation. In this connection, it has been shown that for fiber-dominated modes, the behavior of the fiber-reinforced elastomers—as predicted by the second-order method—is controlled primarily by the *contrast* between the (matrix and fiber) phases and the fiber *volume fraction*. On the other hand, for matrix-dominated modes of deformation, the overall material behavior is controlled by the *in-plane distribution* and *volume fraction* of the fibers—provided that the fibers are sufficiently stiffer than the elastomeric matrix phase.

Similar to other elastomeric systems subjected to finite deformations (see, e.g., Lopez-Pamies and Ponte Castañeda, 2006b; Lopez-Pamies and Ponte Castañeda, in press-b; Michel et al., in press), the predictions generated in this work indicate that the evolution of the underlying microstructure has a very significant and subtle effect on the mechanical response of fiber-reinforced elastomers. In this case, it has been observed that the evolution of the *distribution* of the fibers produces significant geometric stiffening/softening of the effective response of these materials. In particular, it has been observed that when neighboring fibers get closer together (farther apart) in a given direction, the effective incremental response of the material stiffens (softens) in that same direction. At the same time—and more importantly—neighboring fibers getting closer (farther) in a given direction do also lead to the softening (stiffening) of the effective incremental shear response of the material perpendicular to that direction. This latter behavior has been shown to have strong consequences for the macroscopic stability of fiber-reinforced elastomers.

Finally, it is important to emphasize that a major strength of the proposed constitutive model is that it can lose strong ellipticity—even in the case when the underlying matrix phase material and fibers are taken to be strongly elliptic—for loading conditions for which macroscopic instabilities are expected to occur from physical evidence (Kyriakides et al., 1995) and numerical simulations (Triantafyllidis et al., 2006). More remarkably, the specific failure modes by which the estimate loses strong ellipticity depend very critically on the applied loading conditions. Thus, for *out-of-plane* loading conditions with compressive deformation in the fiber direction, the constitutive model loses strong ellipticity in a way that is consistent with the possible development of kink-band-type instabilities. On the other hand, for *in-plane* loading conditions, as well as for mixed *in-plane* and *out-of-plane* conditions with tensile deformation in the fiber direction, the constitutive model loses strong ellipticity in a way that is consistent with the breaking of the symmetries of the underlying, highly ordered, periodic microstructure.

Acknowledgement

The work of O.L.P. and P.P.C. was supported by DOE Grant DE-FG02-04ER46110. Financial support of the Egide program (M.B.) is also gratefully acknowledged.

Appendix A. The microstructural tensor \mathbf{P}

In this appendix, we provide explicit expressions for the components of the microstructural tensor \mathbf{P} , which serves to characterize the two types of microstructures, in the reference configuration, considered in this work:

(a) periodic square, and (b) periodic hexagonal arrangements of monodisperse, aligned cylindrical fibers with initially circular cross section (see Fig. 2 in the main body of the text).

A.1. Periodic square distribution

For the periodic square distribution, the base vectors \mathbf{A}_i ($i = 1, 2, 3$) in (24) are given by $\mathbf{A}_1 = d\mathbf{e}_1, \mathbf{A}_2 = d\mathbf{e}_2, \mathbf{A}_3 = \infty\mathbf{e}_3$, so that expression (21) for \mathbf{P} specializes to:

$$P_{ijkl} = \frac{1}{\pi(1-c_0)} \sum_{p=-\infty}^{+\infty} \sum_{q=-\infty}^{+\infty} N_{ik} \xi_j \xi_l \frac{J_1^2(2\sqrt{\pi c_0} \sqrt{p^2 + q^2})}{p^2 + q^2}, \quad (48)$$

$-\{p = q = 0\}$

where $\xi_1 = p, \xi_2 = q$, and it is recalled that $\mathbf{N} = \mathbf{K}^{-1}$ with $K_{ik} = L_{imkn}^{(1)} \xi_m \xi_n$, and $J_1(\cdot)$ is the Bessel function of first kind. Note that, in terms of the initial radius of the fibers, R , and the unit cell dimension, d , the initial volume fraction of the fibers is given by $c_0 = \pi(R^2/d^2)$.

A.2. Periodic hexagonal distribution

For the periodic hexagonal distribution, the base vectors \mathbf{A}_i ($i = 1, 2, 3$) in (24) are given by $\mathbf{A}_1 = d\mathbf{e}_1, \mathbf{A}_2 = d/2\mathbf{e}_1 + \sqrt{3}d/2\mathbf{e}_2, \mathbf{A}_3 = \infty\mathbf{e}_3$, so that expression (21) for \mathbf{P} specializes to:

$$P_{ijkl} = \frac{\sqrt{3}}{2\pi(1-c_0)} \sum_{p=-\infty}^{+\infty} \sum_{q=-\infty}^{+\infty} N_{ik} \xi_j \xi_l \frac{J_1^2(\frac{2^{3/2}}{\sqrt{3}^{1/4}} \sqrt{\pi c_0} \sqrt{p^2 - pq + q^2})}{p^2 - pq + q^2}, \quad (49)$$

$-\{p = q = 0\}$

where $\xi_1 = p, \xi_2 = \sqrt{3}/3(2q - p)$. Note that, in terms of the initial radius of the fibers, R , and the unit cell dimension, d , the initial volume fraction of the fibers is given by $c_0 = 2\pi/\sqrt{3}(R^2/d^2)$.

References

- Bischoff, E.J., Arruda, E.M., Grosh, K., 2002. A microstructurally based orthotropic hyperelastic constitutive law. *J. Appl. Mech.* 69, 570–579.
- Braides, A., 1985. Homogenization of some almost periodic coercive functionals. *Rend. Acc. Naz.* XL 9, 313–322.
- deBotton, G., Hariton, I., Socolsky, E.A., 2006. Neo-Hookean fiber-reinforced composites in finite elasticity. *J. Mech. Phys. Solids* 54, 533–559.
- Finlay, H.M., Whittaker, P., Canham, P.B., 1998. Collagen organization in branching region of human brain arteries. *Stroke* 29, 1595–1601.
- Gent, A.N., 1996. A new constitutive relation for rubber. *Rubb. Chem. Technol.* 69, 59–61.
- Geymonat, G., Müller, S., Triantafyllidis, N., 1993. Homogenization of nonlinearly elastic materials, microscopic bifurcation and macroscopic loss of rank-one convexity. *Arch. Rat. Mech. Analysis* 122, 231–290.
- Guo, Z.Y., Peng, X.Q., Moran, B., 2006. A composites-based hyperelastic constitutive model for soft tissue with application to the human annulus fibrosus. *J. Mech. Phys. Solids* 54, 1952–1971.
- Hashin, Z., 1962. The elastic moduli of heterogeneous materials. *J. Appl. Mech.* 29, 143–150.
- Hill, R., 1972. On constitutive macro-variables for heterogeneous solids at finite strain. *Proc. R. Soc. Lond. A* 326, 131–147.
- Honeker, C.C., Thomas, E.L., 1996. Impact of morphological orientation in determining mechanical properties in triblock copolymers. *Chem. Mater.* 8, 1702–1714.
- Honeker, C.C., Thomas, E.L., Albalak, R.J., Hadjuk, D.A., Gruner, S.M., Capel, M.C., 2000. Perpendicular deformation of a near-single crystal triblock copolymer with a cylindrical morphology. I. Synchrotron SAXS. *Macromolecules* 33, 9395–9406.
- Horgan, C.O., Saccamandi, G., 2005. A new constitutive theory for fiber-reinforced incompressible nonlinearly elastic solids. *J. Mech. Phys. Solids* 53, 1985–2015.
- Kittel, C., 1968. *Introduction to solid state physics*. John Wiley, New York.
- Knowles, J.K., Sternberg, E., 1975. On the ellipticity of the equations of nonlinear elastostatics for a special material. *J. Elasticity* 5, 341–361.
- Kyriakides, S., Arseculeratne, R., Perry, E.J., Liechti, K.M., 1995. On the compressive failure of fiber reinforced composites. *Int. J. Solids Struct.* 32, 689–738.
- Kyriakides, S., Ruff, A.E., 1997. Aspects of the failure and postfailure of fiber composites in compression. *J. Compos. Mater.* 31, 1633–1670.

- Lahellec, N., Mazerolle, F., Michel, J.C., 2004. Second-order estimate of the macroscopic behavior of periodic hyperelastic composites: theory and experimental validation. *J. Mech. Phys. Solids* 52, 27–49.
- Lopez-Pamies, O., 2006. On the effective behavior, microstructure evolution, and macroscopic stability of elastomeric composites. Ph.D. Dissertation, University of Pennsylvania, USA.
- Lopez-Pamies, O., Ponte Castañeda, P., 2004. Second-order estimates for the macroscopic response and loss of ellipticity in porous rubbers at large deformations. *J. Elasticity* 76, 247–287.
- Lopez-Pamies, O., Ponte Castañeda, P., 2006a. On the overall behavior, microstructure evolution, and macroscopic stability in reinforced rubbers at large deformations: I—Theory. *J. Mech. Phys. Solids* 54, 807–830.
- Lopez-Pamies, O., Ponte Castañeda, P., 2006b. On the overall behavior, microstructure evolution, and macroscopic stability in reinforced rubbers at large deformations: II—application to cylindrical fibers. *J. Mech. Phys. Solids* 54, 831–863.
- Lopez-Pamies, O., Ponte Castañeda, P., in press-a. Homogenization based constitutive models for porous elastomers and implications for macroscopic instabilities: I—analysis. *J. Mech. Phys. Solids*, doi:10.1016/j.jmps.2007.01.007.
- Lopez-Pamies, O., Ponte Castañeda, P., in press-b. Homogenization based constitutive models for porous elastomers and implications for macroscopic instabilities: II—results. *J. Mech. Phys. Solids*, doi:10.1016/j.jmps.2007.01.008.
- Merodio, J., Pence, T.J., 2001a. Kink surfaces in a directionally reinforced neo-Hookean material under plane deformation: I. Mechanical equilibrium. *J. Elasticity* 62, 119–144.
- Merodio, J., Pence, T.J., 2001b. Kink surfaces in a directionally reinforced neo-Hookean material under plane deformation: II. Kink band stability and maximally dissipative band broadening. *J. Elasticity* 62, 145–170.
- Merodio, J., Ogden, R.W., 2003. Instabilities and loss of ellipticity in fiber-reinforced nonlinearly elastic solids under plane deformation. *Int. J. Solids Struct.* 40, 4707–4727.
- Merodio, J., Ogden, R.W., 2005. Mechanical response of fiber-reinforced incompressible nonlinear elastic solids. *Int. J. Nonlinear Mech.* 40, 213–227.
- Michel, J.-C., Lopez-Pamies, O., Ponte Castañeda, P., Triantafyllidis, N., in press. Microscopic and macroscopic instabilities in finitely strained porous elastomers. *J. Mech. Phys. Solids*, doi:10.1016/j.jmps.2006.11.006.
- Müller, S., 1987. Homogenization of nonconvex integral functionals and cellular elastic materials. *Arch. Rat. Mech. Analysis* 99, 189–212.
- Nemat-Nasser, S., Iwakuwa, T., Hejazi, M., 1982. On composites with periodic structure. *Mech. Mater.* 1, 239–267.
- Ogden, R., 1978. Extremum principles in non-linear elasticity and their application to composites—I theory. *Int. J. Solids Struct.* 14, 265–282.
- Ogden, R., 1984. Non-linear elastic deformations. Ellis Horwood, Chichester.
- Ponte Castañeda, P., 1989. The overall constitutive behavior of nonlinearly elastic composites. *Proc. R. Soc. Lond. A* 422, 147–171.
- Ponte Castañeda, P., 2002. Second-order homogenization estimates for nonlinear composites incorporating field fluctuations: I-theory. *J. Mech. Phys. Solids* 50, 237–257.
- Ponte Castañeda, P., Tiberio, E., 2000. A second-order homogenization procedure in finite elasticity and applications to black-filled elastomers. *J. Mech. Phys. Solids* 48, 1389–1411.
- Quapp, K.M., Weiss, J.A., 1998. Material characterization of human medial collateral ligament. *J. Biomech. Eng.* 120, 757–763.
- Qiu, G.Y., Pence, T.J., 1997. Remarks on the behavior of simple directionally reinforced incompressible nonlinearly elastic solids. *J. Elasticity* 49, 1–30.
- Skaggs, D.L., Weidenbaum, M., Iatridis, J.C., Ratcliffe, A., Mow, V.C., 1994. Regional variation in tensile properties and biochemical composition of the human lumbar annulus fibrosus. *Spine* 19, 1310–1319.
- Spencer, A.J.M., 1972. *Deformations of Fibre-reinforced Materials*. Oxford University Press, Oxford.
- Spencer, A.J.M., 1984. *Continuum Theory of the Mechanics of Fibre-reinforced Composites*. Springer, Wein, New York.
- Suquet, P., 1990a. Une méthode simplifiée pour le calcul des propriétés élastiques de matériaux hétérogènes à structure périodique. *C. R. Acad. Sci., Paris Sér. IIb* 311, 769–774.
- Suquet, P. 1990b. Méthodes de calcul simplifiées pour la détermination des propriétés élastiques linéaires de composites à structure périodique. Internal Report, L.M.A., Marseille.
- Triantafyllidis, N., Abeyaratne, R.C., 1983. Instability of a finitely deformed fiber-reinforced elastic material. *J. Appl. Mech.* 50, 149–156.
- Triantafyllidis, N., Maker, B.N., 1985. On the comparison between microscopic and macroscopic instability mechanisms in a class of fiber-reinforced composites. *J. Appl. Mech.* 52, 794–800.
- Triantafyllidis, N., Bardenhagen, S.G., 1996. The influence of scale size on the stability of periodic solids and the role of associated higher order gradient continuum models. *J. Mech. Phys. Solids* 44, 1891–1928.
- Triantafyllidis, N., Nestorvić, M.D., Schraad, M.W., 2006. Failure surfaces for finitely strained two-phase periodic solids under general in-plane loading. *J. Appl. Mech.* 73, 505–515.